"Structural Health Monitoring of civil infrastructures, using both GPS-Galileo HAS and accelerometric data"

Decreto Del Capo Dipartimento Rep. n. 2 Prot. n.35 del 13/01/2021

Report on the activities carried out for the European project GISCAD-OV during 2022/2023

Università degli Studi Roma Tre

Dipartimento di Architettura

Responsabile del progetto: Dott. S. Gabriele

Assegnista di ricerca: Ing. Daniele Cinque

Roma, 28/02/2023

Table of contents

Index of figures

Index of tables

1 Introduction

The present report is intended to describe the activities carried out by Daniele Cinque as a Research Fellow of the Department of Architecture of Rome Tre University in the period from March 2022 to February 2023. The activities carried out were part of the European project GISCAD-OV (Galileo Improved Services for Cadastral Augmentation Development On-field Validation) and the main aim was to study the effectiveness of a multi-GNSS-based monitoring system for civil infrastructures (1,2). The system is based on the integration of GPS and the Galileo High Accuracy System (HAS), exploiting advanced RTK and PPP-AR techniques, with an update rate up to 100 Hz. The work was developed by the joint effort of the University Roma Tre (UNIROMA3), the Italian Department of Civil Protection (DPC) and the Italian ICT company SOGEI.

The current state of the art shows that in the SHM field, accelerometers are widely used. By processing the acquired accelerations, the displacements and the frequency content can be evaluated and used to obtain parameters to assess the integrity of the monitored structure (3,4). However, the great limitation is the numerical error that the process suffers from, induced by the experimental noise and the sampling frequency. Indeed, the displacements are calculated via the double numerical integration of the accelerations and the frequency content by applying a fast Fourier transform-based algorithm to the signal. A possible advantage of using a GNSS-based monitoring system is that it allows a direct measurement of the displacements and therefore improves the double integration conditioning. As an example, such kinds of measurement can be used to calculate the relative displacements and inter-floor drifts in order to obtain the parameters for the assessment of the state of the structure. Current applications of the GNSS-based monitoring system (also exploiting advanced PPP technologies), with a sampling frequency up to 100 Hz, also allow us to fully cover the frequency range of interest in seismic applications, which is limited to between 0.1 Hz and 15 Hz (5–9). Moreover, the proposed technology allows us to measure both static and dynamics displacements, contrary to terrestrial systems, which are distinct for the two types of measurements (10,11). The system will be a cost-effective solution for monitoring structures that are not endowed

with a terrestrial monitoring system (12,13). The last great advantage is that it will be useful in case of the unavailability of terrestrial communication links as well as for continuous monitoring in infrastructure monitoring applications (14–16).

The current state of the art of GNSS-based SHM systems shows that is possible to exploit RTK and standard PPP techniques basically carried out in a post-processing mode on controlled infrastructures (17–19). The work here presented focuses on the application of real-time GNSS PPP-RTK high-accuracy techniques for operative infrastructure monitoring (e.g., bridge monitoring), paving the way for the use of the Galileo HAS, a fully satellite-based positioning service. The efficiency and accuracy of the system were tested during the activities carried out from March 2021 to February 2022, of which a detailed description is presented in the 2021/2022 final report that describes the activities of Daniele Cinque as a Research Fellow for the Department of Architecture of Roma Tre University in the period from March 2021 to February 2022. The test was carried out on a small-scale benchmark structure through a comparative analysis based on the results obtained by an accelerometric monitoring system, installed by the Italian Department of Civil Protection (DPC), and a Finite Element Model (FEM) of the structure, implemented by UNIROMA3. The latter was implemented thanks to a 3D survey conducted on the structure by means of a laser scan. The comparative analysis is in both the frequency and time domain. Hence, the main goal of the test was to obtain the principal vibration frequencies of the tested structure from the GPS+Galileo HAS system, the accelerometric system and the FEM model and to obtain the estimation of the maximum amplitude displacements, that could be further used as indicators for structural safety, from both the monitoring systems. From the comparison in the time domain, the events captured by the accelerometric and GNSS systems were perfectly synchronized and of almost the same entity with an average difference of about 5mm. From the comparison in the frequency domain, the absolute frequency shifts of the GNSS and accelerometric systems were comparable with a tolerance of less than 5%. The difference in the frequency domain between the GNSS system and the FEM is about the 10%. Moreover, a statistical analysis of the satellite noise was carried out showing that the minimal sensible displacement of the GNSS is of about 5 mm and 2 mm

in the vertical and horizontal plane respectively. All the results of the test are reported in the annex of the present report.

The same methodology was then applied in the validation on a road bridge carried out from March 2022 to February 2023, which is described in the present report. The main difference between the test and the validation is that the displacements of interest of the benchmark structure were those in the plane tangent to the surface of the earth. In the validation, the GNSS-based structural monitoring was applied to a road bridge under normal traffic conditions. Hence, the displacements of interest were those in the plane orthogonal to the surface of the Earth. In order to assess the accuracy of the GNSS, the structure was also monitored by means of accelerometers. The results acquired by the two types of monitoring systems were then compared only in the time domain since due to the nature of the structure and the excitation, it was not possible to evaluate the natural frequency of the structure. Moreover, due to the complexity of the structure it was decided not to implement a FEM.

The work is also described in the conference paper “Application of innovative High Accuracy GNSS based system to the monitoring of civil structures”, published in the 10th European Workshop in Structural Health Monitoring that was held in 2022 in Palermo, and in the journal paper “Experimental Validation of a High Precision GNSS System for Monitoring of Civil Infrastructures”, published in the journal Sustainability by MDPI in 2022. The work was also presented at the final technical meeting of GISCAD-OV, held in the Department of Architecture of Delft University in 2023.

2 Background knowledge

2.1 Geodetic coordinates and geodetic datums

The position acquired by the satellite system is in geodetic coordinates which are calculated in the Earth Centred-Earth Fixed geodetic (ECEF-g) reference system, the customary reference for the GNSS (20). The coordinates for this frame are the geodetic latitude, longitude and height. The first two, which are referred to as ϕ and λ, respectively, are angular distances that specify the horizontal position of the point of interest on the surface of the earth. The third one, which is referred to as h, is the elevation of the point of interest above the surface of the earth. Therefore, geodetic coordinates are defined relatively to a particular Earth geodetic datum, which is a means of representing the figure of the Earth (21). The geodetic datum is usually an oblate ellipsoid of revolution that approximates the surface of the Earth, being characterized by a semimajor and semiminor axis. The ellipsoid can be easily obtained considering a Cartesian reference system. The revolution of the ellipsoid is about the polar axis Z while the axes X and Y are positioned in order that the positive X-axis defines zero longitude while the positive Y-axis is chosen to complete an orthogonal right-handed coordinate system (22). This Cartesian reference system with origin O in the centre of the ellipsoid is usually referred to as Earth Centred-Earth Fixed rectangular (ECEF-r) reference system. Once the geodetic datum in specified, the geodetic coordinates can be defined relatively to the ECEF-g reference system. Latitude ϕ is defined as the angle between the ellipsoidal normal through the point of interest and the equatorial plane. Longitude λ is defined as the angle between the meridian that contains the point of interest and the Prime meridian, also known as Greenwich meridian. Finally, height h is defined as the elevation of the point of interest above the surface of the ellipsoid. Since the geodetic coordinates are measured relative to a fixed point on the surface of the earth, ECEF-g rotates at the earth rate, i.e., it is a non-inertial frame.

Figure 1 displays both the reference systems introduced so far. Figure 2 and Figure 3 show how to calculate the geodetic coordinates. Since the geodetic datum is an ellipsoid, the ellipsoidal normal through point P does not cross the origin of the reference system unlike what happens when a sphere is considered.

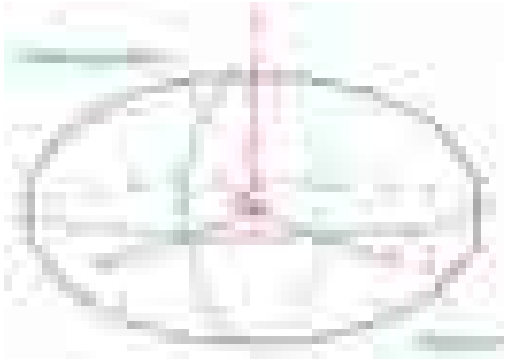

Figure 1. Ellipsoid showing the ECEF-g (in blue) and the ECEF-r (in red) reference systems.

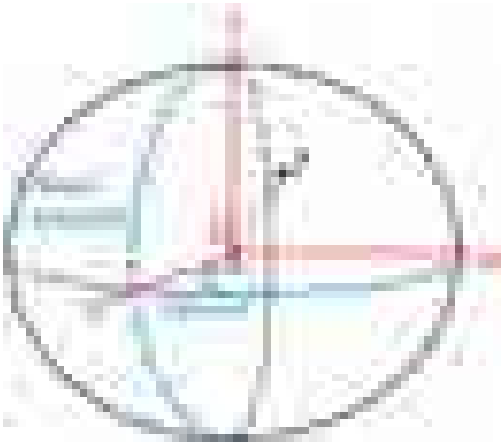

Figure 2. Ellipsoid showing ECEF-g and ECEF-r reference systems, the ellipsoidal normal through point P and the geodetic longitude of P.

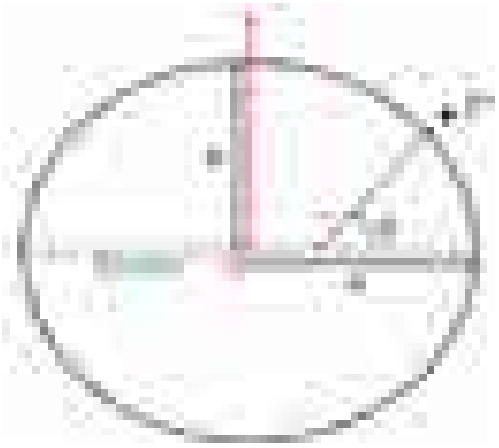

Figure 3. Meridian plane containing point P showing the ellipsoidal normal through P, the geodetic latitude of P, the ellipsoidal height of P and both the semiminor and semimajor axis of the ellipsoid, b and a, respectively.

Since the geodetic coordinates are dependent on the geodetic datum, they will differ between datums. The geodetic datum that is adopted in the present work is known as WGS84 (World Geodetic System 1984) and it is geometrically defined as follows:

$$Semimajor\ axis \qquad a = 6378137.000000\ m$$

$$Semiminor\ axis \qquad b = 6356752.314245\ m$$

$$Flatness \qquad f = \frac{a-b}{a} = 3.3528107 \times 10^{-3}$$

$$Eccentricity \qquad e = \sqrt{f(2-f)} = 8.1818191$$

$$Normal\ radius\ of\ curvature \qquad N(\phi) = \frac{a}{\sqrt{1 - e^2 \sin^2(\phi)}}$$

Figure 4 displays the meridian plane of the ellipsoid that contains the point of interest P together with the geometrical features of the ellipsoid. In particular, the normal radius of curvature N is graphically defined as the distance along the ellipsoid normal between the vertical projection of P on the ellipsoid surface and the semiminor axis b.

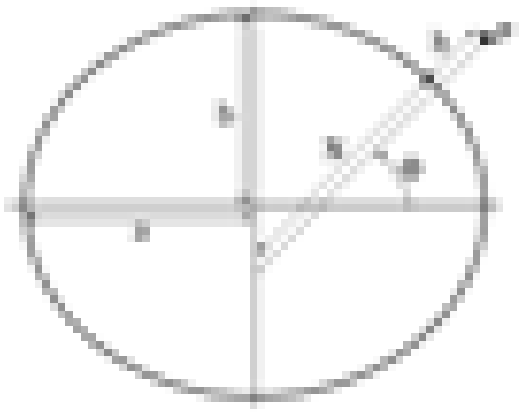

Figure 4. The geodetic ellipsoid showing the semimajor and semiminor axes (a, b), the height (h), the latitude (λ) and the plumb line from the point of interest P to the z axis.

2.2 Geodetic coordinates transformation

The data acquired by the GNSS system is organized in WGS84 geodetic coordinate system. On the other hand, the accelerometers' signal is organized in its local coordinate system, which means that the coordinate system depends on the position chosen for the accelerometer during the installation process. Since the displacements of the tested structure that we were interested in were the out-of-plane displacements, the accelerometers were installed accordingly to the local reference system of the structure. Therefore, the local coordinate system refers to the tested structure. In order to be able to compare the two set of data, one needs to express the signals of both the GNSS and the accelerometric system in a common coordinate system. This is why there is the necessity to apply coordinate transformation equations. For this purpose, it has been decided to consider the local coordinate system of the tested structure as reference. Hence, the accelerometers do not need to be transformed unlike the satellite signal. The

straightforward method to convert the geodetic coordinates to local coordinates involves three different coordinate transformations. The first one involves a coordinate conversion from the ECEF-g to the ECEF-r reference system. Equations (1-3) that are explained in the work by Heiskanen and Moritz (23), allow this transformation.

$$X = (h + N)\cos\phi\cos\lambda \quad (1)$$

$$Y = (h + N)\cos\phi\sin\lambda \quad (2)$$

$$Z = (h + (1 - e^2)N)\sin\phi \quad (3)$$

Once the coordinates are in the ECEF-r frame, there is the necessity to apply a second transformation in order to obtain a tangent plane coordinate system, known as East-North-Up reference system (ENU). It is still a Cartesian system but the first two coordinates' axes are in the plane tangent to the surface of the ellipsoid. Therefore, these two axes define the ellipsoid tangent plane rather than the equatorial plane as in the ECEF-r reference system. The origin O' is a reference point in the region of interest. This may be on the ellipsoidal surface, or above or below it. The axis Z' is the ellipsoidal normal through O', so it is approximately the local vertical. The plane that contains the axes X' and Y' is perpendicular to the Z'-axis, so it is approximately horizontal in the area. The three axes X', Y' and Z' identify an orthogonal right-handed coordinate system and they point towards east, north and up respectively. This is why, for this work it was decided to adopt the nomenclature of E, N and U for the X', Y' and Z' respectively. The three different coordinate systems are shown in Figure 5.

Figure 5. A schematic diagram for the WGS84, ECEF, and ENU coordinate systems for the Earth and their transformation relationships (PM line is the Prime Meridian; ϕ and λ are latitude and longitude in WGS84; X,Y,Z for ECEF; and E,N,U for ENU) (24).

The great advantage of the ENU system is that its axes coincide with the expectation of people on the ground concerning such ingrained things as up, and north, which something like ECEF-r does not (20). The transformation from ECEF-r to ENU can be built up from a sequence of simple translation and rotations, resulting in an orthogonal transformation matrix shown in Equation (4), explained in the work Heiskanen and Moritz (23).

$$\begin{pmatrix} E \\ N \\ U \end{pmatrix} = \begin{pmatrix} -\sin(\lambda) & \cos(\lambda) & 0 \\ -\cos(\lambda)\sin(\phi) & -\sin(\lambda)\sin(\phi) & \cos(\phi) \\ \cos(\phi)\cos(\lambda) & \cos(\phi)\sin(\lambda) & \sin(\phi) \end{pmatrix} \begin{pmatrix} X - X_0 \\ Y - Y_0 \\ Z - Z_0 \end{pmatrix} \quad (4)$$

In the above equation, X_0, Y_0 and Z_0 are the coordinates of the origin O' of the ENU coordinate system expressed in the ECEF-r coordinate system.

Lastly, the data must be organized in the local reference system of the tested structure according to the disposition of the accelerometers. In the present work, the tested structure lay on the ellipsoid tangent plane as shown in Figure 6. Hence, the coordinate transformation involves a 2D rotation about the z-axis, which represents the normal of the

ellipsoid tangent plane. The transformation matrix that is used for a clockwise rotation α is shown in Equation (5).

$$\begin{pmatrix} X_L \\ Y_L \\ Z_L \end{pmatrix} = \begin{pmatrix} \cos(\alpha) & -\sin(\alpha) & 0 \\ \sin(\alpha) & \cos(\alpha) & 0 \\ 0 & 0 & 1 \end{pmatrix} \begin{pmatrix} E \\ N \\ U \end{pmatrix} \quad (5)$$

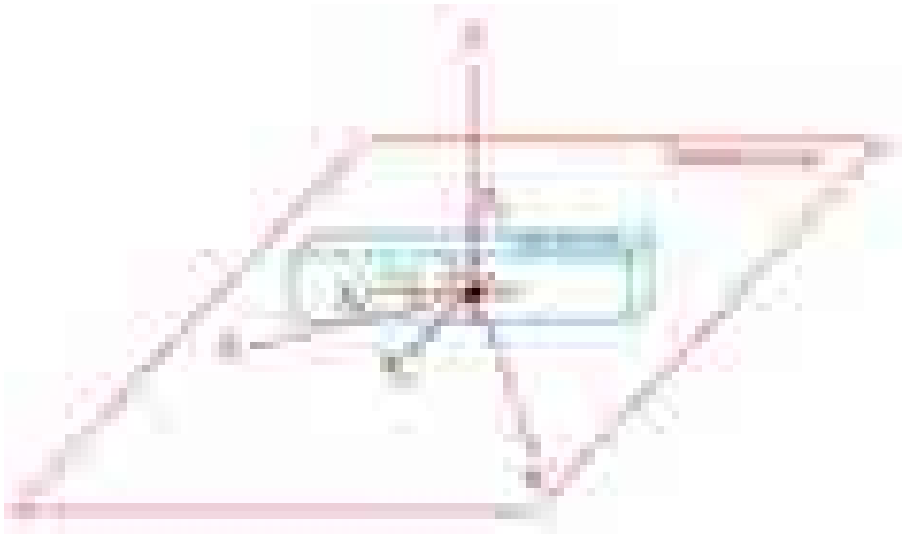

Figure 6. A schematic diagram representing the transformation of coordinates from the ENU (in red) to the local reference system (in black) where latter is referred to the tested structure (in blue). As it can be noticed, the transformation involves a rotation around the z-axis. Therefore, the z-axis of both reference systems define the normal of the ellipsoid tangent plane.

In conclusion, the straightforward method to convert the geodetic coordinates to local coordinates implies a three-step transformation process: a first conversion in ECEF-r, a second in ENU and the last in the local reference system. The four different coordinate systems that were considered in the previous discussion are shown in Figure 7.

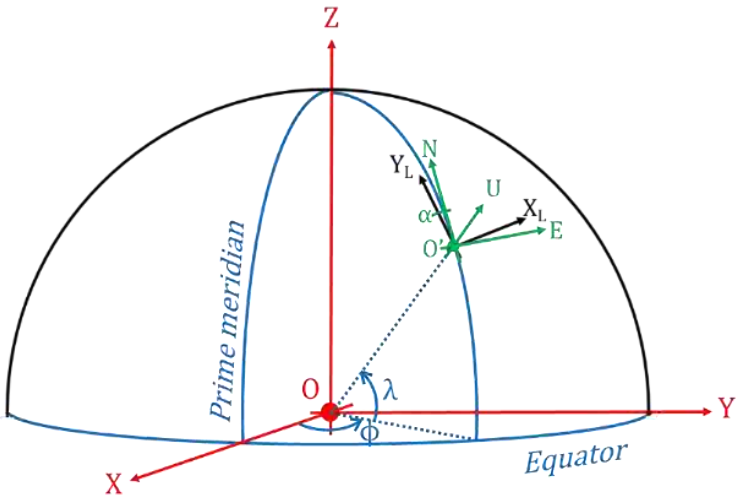

Figure 7. Schematic representation of the ellipsoid showing the four coordinate systems previously considered: ECEF-g (in blue), ECEF-r (in red), ENU (in green) and local (in black).

3 Previous results

The results achieved during the test showed that the GNSS monitoring system was able to describe the dynamic behavior of a benchmark structure, depicted in Figure 8, in the time and frequency domain. Indeed, a monitoring campaign was carried out on a steel framed structure located on the top roof of one of Sogei's buildings. This consisted of monitoring the structure with the provided GNSS system and an accelerometric system that served as baseline.

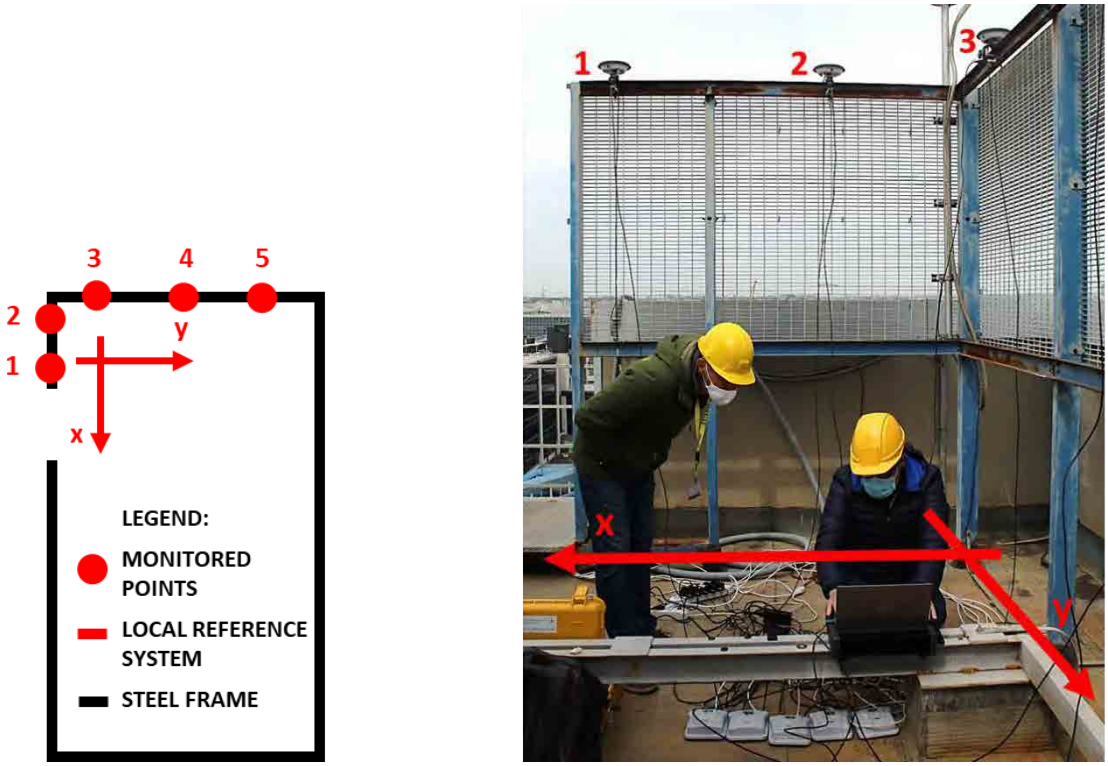

(a) (b)

Figure 8. Benchmark structure monitored during the test: (a) Schematic plan view; (b) GNSS based monitoring system installed on the steel framed structure.

The structure was monitored while a manual excitation was performed in order to give an oscillatory motion to the structure that simulated its behavior during an extraordinary event. The main characteristics of this test were, first, the structure had a very elastic nature, and second, the structure was given a horizontal motion during the test. Therefore, the elastic nature of the structure allowed us to acquire a signal in which the performed excitation was very clear and it was not dissipated immediately, showing a first forced oscillatory motion and then a free oscillatory motion. Moreover, the fact that the excitation was performed in the horizontal plane allowed us to focus only on the horizontal displacements of the structure, avoiding the analysis of the vertical displacements which, according to literature, suffers of a noise of a higher order of magnitude. This last aspect has already been demonstrated in the statistical analysis carried out on the test results. Those characteristics of the test put us in an ideal condition to monitor the structure. Figure 9 shows an example of GNSS signal that was acquired during the test. The signal depicts the displacement along the y-axis of the local reference system of one of the monitored

points of the structure, in the time domain. The signal is very clear and the starting of the manual excitation and the difference between forced and free oscillations can be appreciated. Moreover, it is highlighted the noise the signal suffers from, which has an order of magnitude of a few millimeters.

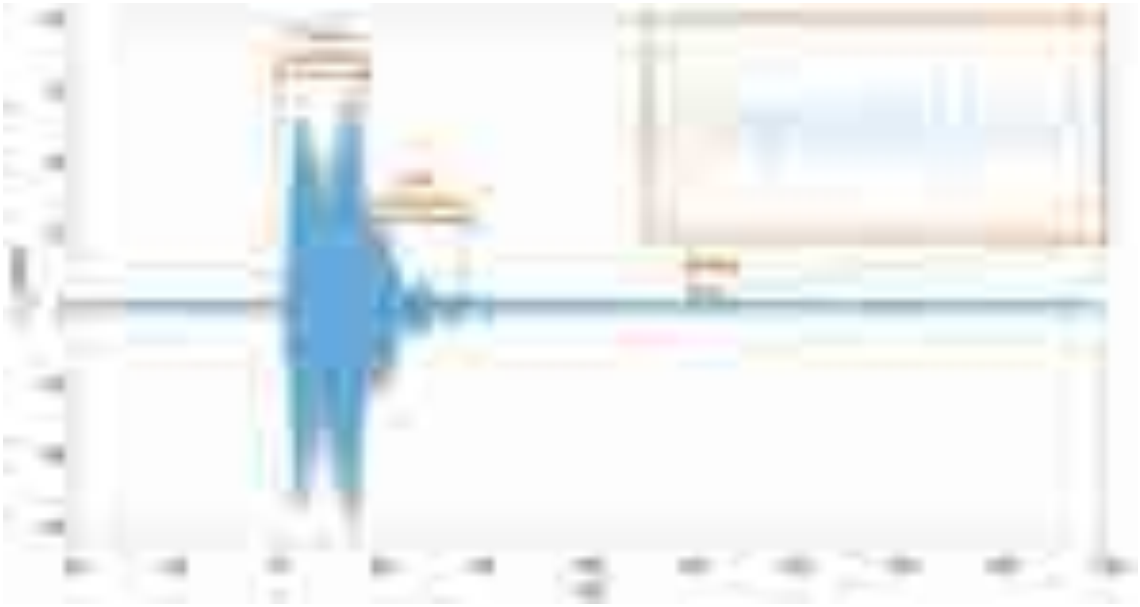

Figure 9. Example of signal acquired during the test.

In this case it was possible to analyze the satellite signal in both the time and frequency domain. To assess the correct functioning of the GNSS system and its accuracy, the results were compared to those acquired by an accelerometric system that served as baseline. The comparison was carried out first in the time domain, by graphically comparing the two profiles and evaluating the peak displacements, as shown in Figure 10.

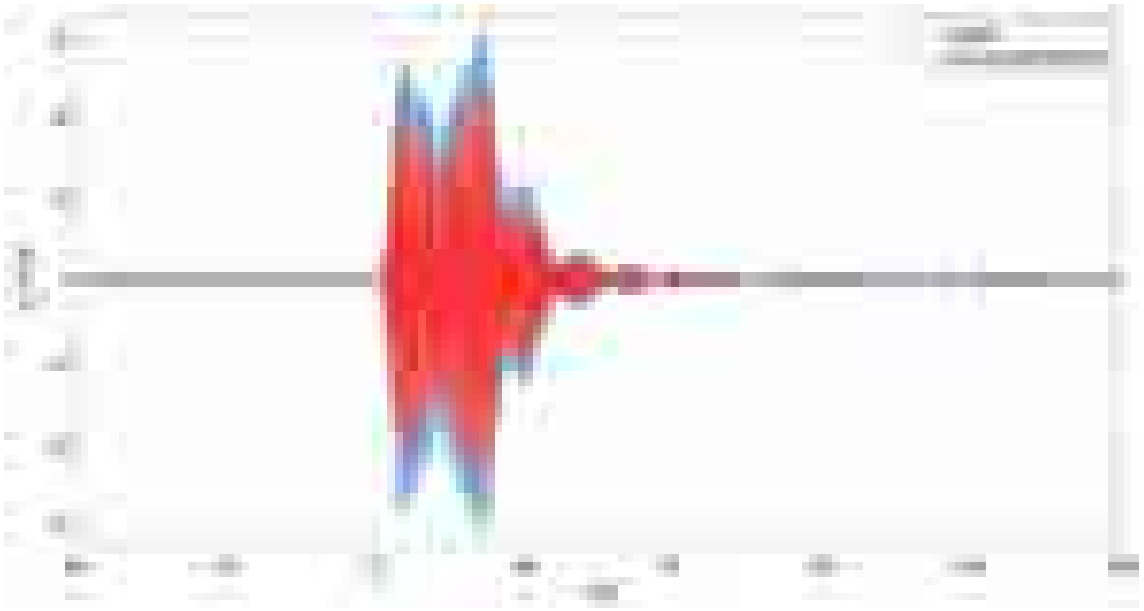

Figure 10. Example of comparison in the time domain between the signals acquired by the GNSS and accelerometric systems.

The signals were also analyzed in the frequency domain by comparing the peak frequencies, which corresponds to the natural frequency of the structure, as shown in Figure 11. The methodology to evaluate the peak frequencies consisted of applying the PSD (Power Spectral Density) to the range of free oscillations of the signals.

Figure 11. Example of comparison in the frequency domain between the signals acquired by the GNSS and the accelerometric systems.

The signals were acquired during four monitoring tests. The first one, without exciting the structure, served to define the displacements' baseline and to analyze the noise. The other tests were carried out with a manual excitation performed on the structure in a precise point of application and direction, as specified in Table 1.

Table 1. Characteristics of the tests that were carried out.

Test	Direction of Excitation	Point of Application
1	-	-
2	y	1
3	x	5
4	y	1

The direction of excitation refers to the axes of the local reference system showed in Figure 8. The point of application refers to the monitored points highlighted in Figure 8. Indeed, the excitation was performed by manually applying a force in a point very close to the first and fifth monitored points in order to make the structure oscillate. The complete results are reported in the annex of the present report.

In order to find out what is the average difference in the time domain between the two monitoring systems, a comparative analysis between the peak displacements acquired was carried out. As reported in Table 2, the average difference, calculated with the results acquired during test 2, 3 and 4, is about 5mm. The reported results were evaluated without considering the GNSS receiver that monitored point 3, which did not give satisfying results. The results reported in the below table were roughly expected due to the minimal sensible displacement that was calculated through the statistical analysis. Indeed, this analysis led to a horizontal minimal sensible displacement due to noise of about +/-2mm.

Table 3 shows the results of the comparative analysis in the frequency domain. The GNSS system managed to identify almost the same natural frequency of the accelerometric system. The difference, without considering GNSS 3, is less than the 1%.

The detailed results of the test are reported in the annex.

Table 2. Results in the time domain of the test.

Test	**Difference of peak displacements**	
[-]	[mm]	[%]
2	4.9	27.3
3	6.3	26.5
4	4.7	22.8
Average	5.3	25.5

Table 3. Results in the frequency domain of the test.

Test	**Frequency**			
	GNSS	Acc.	Diff.	Diff.
[-]	[Hz]	[%]	[Hz]	[%]
2	4.46	4.50	0.04	0.89
3	4.30	4.30	0.00	0.00
4	4.13	4.13	0.00	0.00
Average	4.30	4.31	0.01	0.30

4 Structure description

In order to validate the results achieved in the test, a monitoring campaign was conducted on a real case scenario, that is a road bridge, managed by the national company ANAS s.p.a. Figure 12 and Figure 13 shows two different views of the structure. The road bridge is part of the two-lane national road SS675 that crosses the river Tiber in a location sited near the city of Orte at the north of Rome, in the county of Viterbo, in the Italian region Lazio. The multi-span road bridge counts a total of 33 spans, it is made of prestressed concrete and its deck is composed of four box girders. A schematic cross section of the bridge deck is depicted in Figure 14. The cross section of the girders is depicted in Figure 15. Different views from beneath the bridge are shown in Figure 16 and Figure 17.

Figure 12. Longitudinal drone view of the road bridge.

Figure 13. Transversal drone view of the road bridge.

Figure 14. Schematic view of the cross section of the bridge deck (courtesy of ANAS s.p.a.).

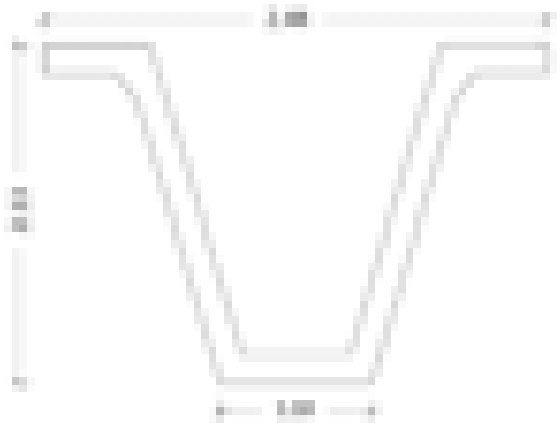

Figure 15. Schematic representation of the cross section of the girder, units in meters.

Figure 16. Details of the connection between the second and the third span.

(a) (b)

Figure 17. (a) View of the second span from beneath; (b) view of the monitored lane (Viterbo direction) from beneath.

5 Monitoring system installation

The GNSS system was installed on the second span of the bridge, on the lane directed to Viterbo, and was set to acquire in continuous under normal traffic conditions. Three GNSS sensors were available at the time of the campaign. The setup points were chosen according to the principal bending mode shapes of the structure, which static system is represented by a simply supported beam, 40m long, with weight considered as a distributed load. Figure 18 shows the schematic two principal bending mode shapes of the structure. Figure 19 shows the second span of the bridge and setup points of the GNSS sensors. The installation of the monitoring system was carried out thanks to ANAS s.p.a., the national company that has in charge the management of the structure. The road was partially closed to traffic in order to secure the staff during the installation, as shown in Figure 20.

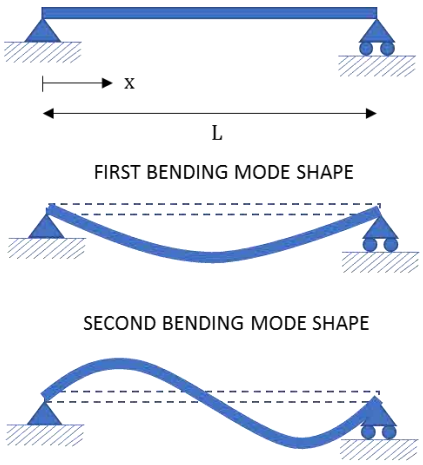

Figure 18. First two bending mode shapes of a simply supported beam.

Figure 19. View of the second span of the bridge, being the monitored points highlighted.

Figure 20. Installation of a GNSS antenna.

For safety reasons the installation points of the monitoring sensors were fixed on the support posts of the guardrail. In order to avoid disturbance of the satellite signal produced by the guardrail itself, the GNSS antennas needed to be installed on the top part of the support posts, as shown in Figure 21. To verify that the dynamic behavior of the top and bottom part of the generic support post, being the latter integrated to the bridge, were the same, the DPC conducted a verification campaign by means of accelerometers. Two temporary accelerometers were installed on the same support post, being one installed on the bottom of the post and one on the top, as shown in Figure 22.

Figure 21. Installation of a GNSS antenna on the top part of the guardrail's support post.

(a) (b)

Figure 22. (a) Accelerometer installed on the top part of the guardrail's support post; (b) accelerometer installed on the bottom part of the guardrail's support post.

Since the structure was monitored under normal traffic conditions, the major displacements were expected to be in the vertical direction. Therefore, the accelerations that were analyzed during the monitoring campaign were those along the z axis in the local reference system, shown in Figure 23. The comparison between the two signals was carried out in the frequency domain. The autospectrum was evaluated for each signal in order to cut off the electric noise that may differ for the two accelerometers. Figure 24 and Figure

25 show the results obtained from the monitoring of two support posts located at the centerline and at a quarter of the span length, respectively. As it can be noticed, the two measurements describe almost the same vertical dynamic behavior.

Figure 23. Local reference system of the road bridge.

Figure 24. Autospectrum of the accelerometric signals acquired from the top and bottom part of the guardrail's support post, located at the centreline of the span.

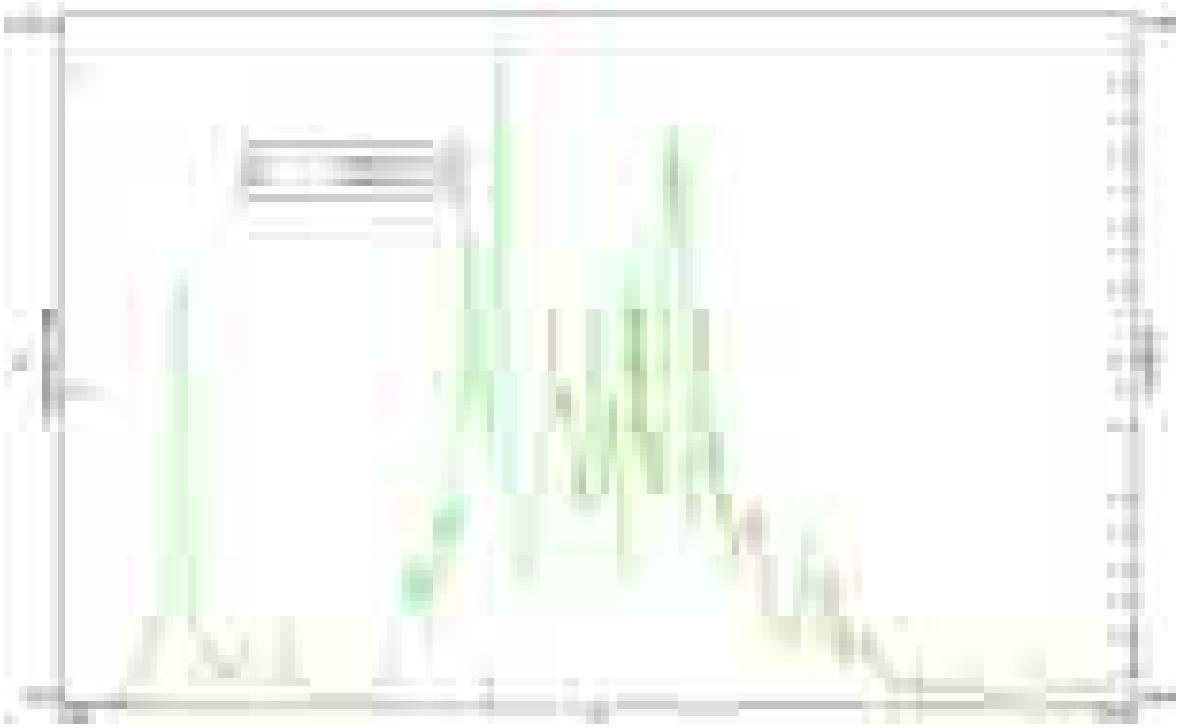

Figure 25. Autospectrum of the accelerometric signals acquired from the top and bottom part of the guardrail's support post, located at a quarter of the span's length.

Once it was assessed that the top and bottom part of the post had the same dynamic behavior along the vertical axis, it was possible to proceed with the installation of the monitor systems ahead of the data acquisition campaign. Due to the availability of the GNSS sensors, three antennas were installed on the road bridge, on the lane directed to Viterbo. Two antennas were mounted at the centerline of the bridge, one on the right-side and one on the left-side of the lane. A third antenna was mounted at a quarter of the span's length, on the right side of the lane. Figure 26 shows a schematic representation of the plan view of the bridge, in which the setup points are highlighted. We will refer to the three GNSS sensors as GNSS1, GNSS2 and GNSS3 from now on.

Since the functioning of the GNSS system was assessed through the test thanks to an extended comparison in the time and frequency domain with the results of an accelerometric system, for task 5.6 it was decided to adopt only one accelerometer. The one accelerometer served as validation of the GNSS acquisitions, since a real case scenario generally shows disturbances of the signal impossible to study through the benchmark structure of the test. The accelerometer was of the force-balance type, with a measurement range from 0 to 200 Hz, and therefore also able to measure the accelerations

caused by quasi-static excitation, and was installed on point number 2 highlighted in Figure 26. Figure 27 shows installation point number 2 on which both the GNSS antenna and the accelerometer were mounted. Figure 28 shows installation point number 1 on which a GNSS antenna was mounted. Both monitoring systems were left in position for about two weeks, acquiring in continuous and organizing data in 1-hour interval measurements.

Figure 26. Schematic representation of the plan view of the second span of the road bridge, being the monitored points highlighted.

Figure 27. Installation point number 2 on which the GNSS antenna and the accelerometer were both mounted.

Figure 28. Installation point number 1 on which the GNSS antenna was mounted.

6 Statistical analysis

As already did for the test (refer to the results reported in the annex), a statistical analysis of the satellite signals was carried out in order to characterize the noise that affects the measurement. Before proceeding with the analysis, the signal was processed in order to obtain filtered displacements in the local reference system of the bridge by applying the same methodology previously explained. The purpose of the analysis is to understand the limit of the minimal sensible displacement that can be acquired by this kind of instrumentation when installed on a road bridge. The results for each GNSS receiver are shown in the next section and follow the same nomenclature of the monitored points, hence, the three GNSS sensors are referred to as GNSS 1, GNSS 2 and GNSS 3. The signal being analyzed refers to the 1-hour acquisition carried out during September 24, 2021, starting at 2:26:04 am.

6.1 GNSS 1

Figure 29 depicts the displacements along the local x, y and z direction acquired by the GNSS signal installed on the first monitored point. For each signal, the mean, the variance and the standard deviation are evaluated. Moreover, the values that delimit the 99^{th} percentile are calculated, so that the outliers due to the crossing of vehicles are not considered. The thresholds of the noise are identified by the quantiles 0.995 and 0.005, respectively. Those values delimit the minimal sensible displacements. As it can be noticed, the minimal sensible displacement changes significantly whether horizontal or vertical displacements are considered.

Figure 29. Displacements acquired by GNSS 1.

Figure 30 depicts the fitting of empirical data by means of a normal distribution. As obtained in the test, the distribution perfectly describes the set of data and is symmetrical with respect to the mean value, which is always zero. As expected, there is a big difference between the shapes of the distributions that fit the horizontal and vertical displacements. While the mean value is always zero, the variance of the vertical displacements is much higher.

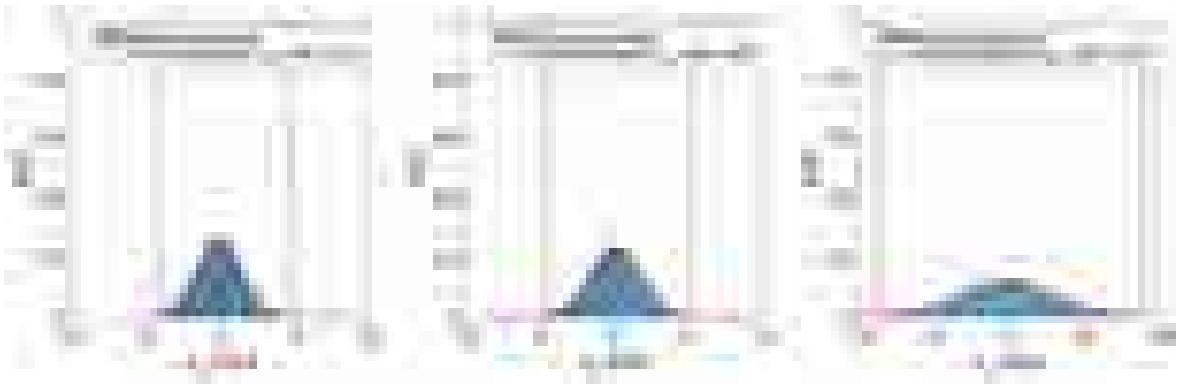

Figure 30. Distributions that fit data acquired by GNSS 1.

Figure 31 shows the position acquired by GNSS 1. The limits of the axes are fixed by the quantiles previously introduced, hence the 99% of data is depicted. In the case of horizontal displacements, the threshold of the minimal sensible displacement is about 4 mm while in

the case of vertical displacements is about 8 mm. Those threshold values were evaluated as the mean of the absolute value of the percentiles.

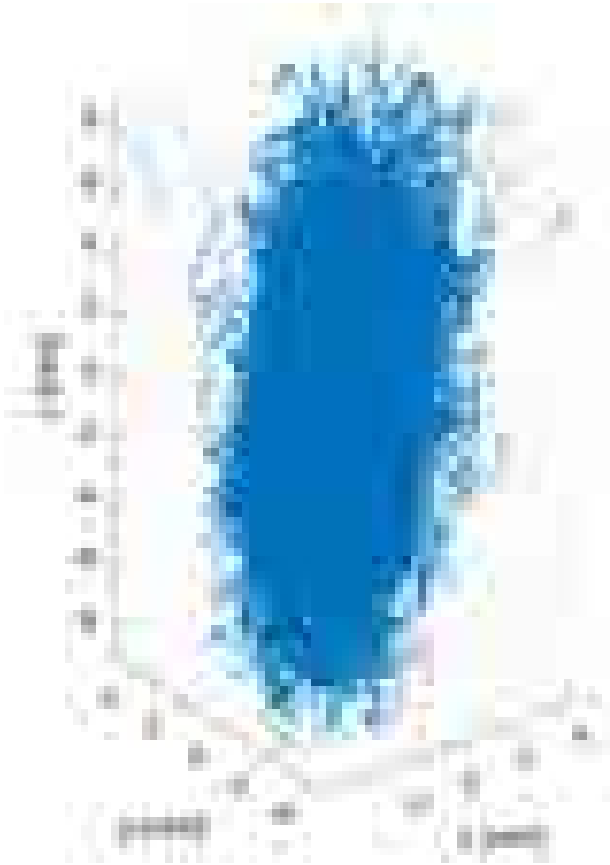

Figure 31. Position acquired by GNSS 1.

The results of the statistical analysis are shown in Table 4. The column “Direction” contains the axes along which the displacements were measured. The values of the variance and the standard deviation are under the columns “Var” and “Std”. The values of the percentiles that delimit the minimal sensible displacements of the system are under the columns “Perc. 99.5%” and “Perc. 0.5%”. The results of the other GNSS receivers follow in the next sections and are shown from Figure 32 to Figure 37.

Table 4. Results of statistical analysis of GNSS 1 signal.

Direction [-]	Mean [mm]	Var [mm^2]	Std [mm]	Perc. 99.5 % [mm]	Perc. 0.5 % [mm]	Threshold [mm]
x	-0.03	2.41	1.55	4.72	-3.98	4.35
y	0.09	3.05	1.75	4.98	-4.59	4.79
z	-0.07	11.37	3.37	8.97	-8.83	8.90

6.2 GNSS 2

Figure 32. Displacements acquired by GNSS 2.

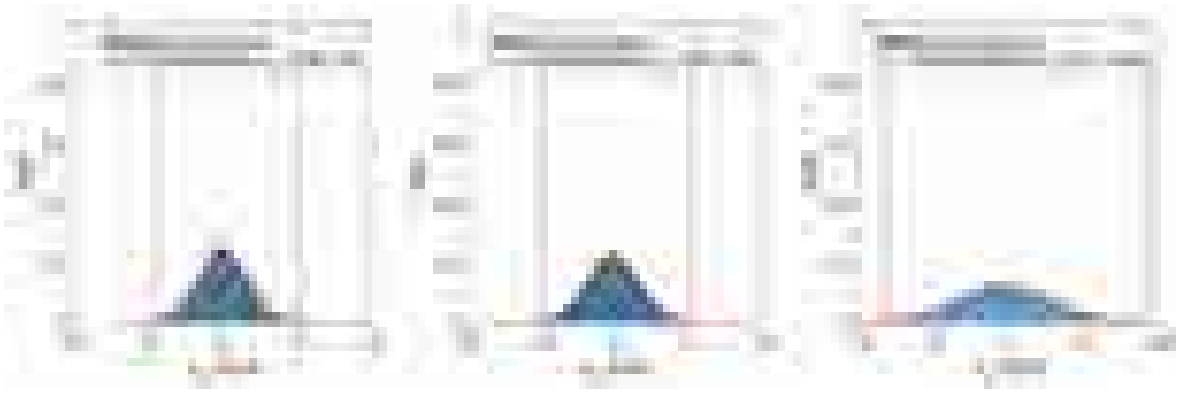

Figure 33. Distributions that fit data acquired by GNSS 2.

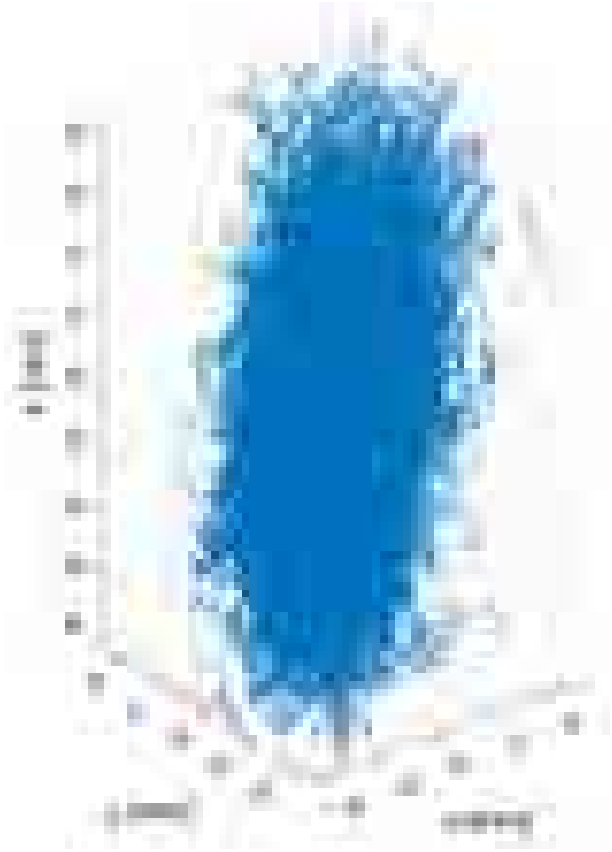

Figure 34. Position acquired by GNSS 2.

Table 5. Results of statistical analysis of GNSS 2 signal.

Direction [-]	**Mean** [mm]	**Var** [mm^2]	**Std** [mm]	**Perc. 99.95 %** [mm]	**Perc. 0.05 %** [mm]	**Threshold** [mm]
x	0.06	2.87	1.70	5.04	-4.32	4.68
y	-0.09	3.29	1.81	4.96	-4.89	4.93
z	-0.17	11.06	3.33	9.26	-8.27	8.77

6.3 GNSS 3

Figure 35. Displacements acquired by GNSS 3.

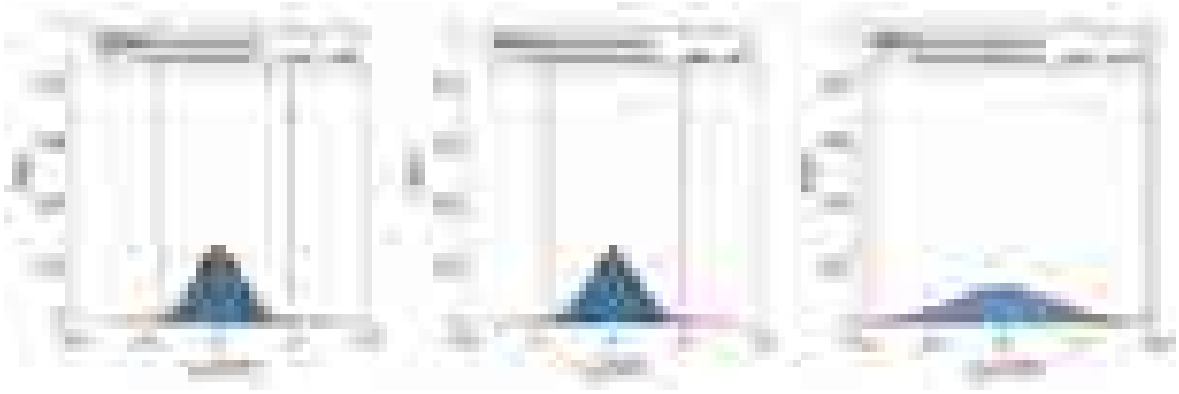

Figure 36. Distributions that fit data acquired by GNSS 3.

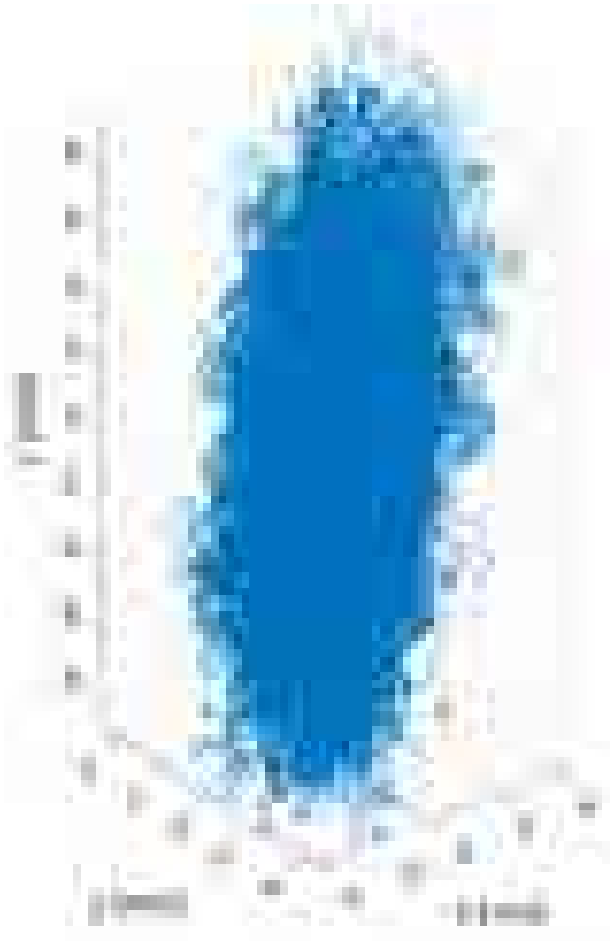

Figure 37. Position acquired by GNSS 3.

Table 6. Results of statistical analysis of GNSS 3 signal.

Direction [-]	**Mean** [mm]	**Var** [mm^2]	**Std** [mm]	**Perc. 99.95 %** [mm]	**Perc. 0.05 %** [mm]	**Threshold** [mm]
x	-0.01	2.59	1.61	4.76	-4.09	4.43
y	0.09	2.91	1.71	4.76	-4.35	4.56
z	-0.04	12.36	3.52	9.65	-9.11	9.38

6.4 Comparison of the GNSS receivers

The normal distributions of the noise obtained from the displacements along the x, y and z local directions for each GNSS receiver are compared in Figure 38. The comparison of the boxplots is shown in Figure 39. The results obtained from the analysis of the displacements for the local x, y and z direction are shown from Table 7 to Table 9.

Figure 38. Comparison of the normal distributions.

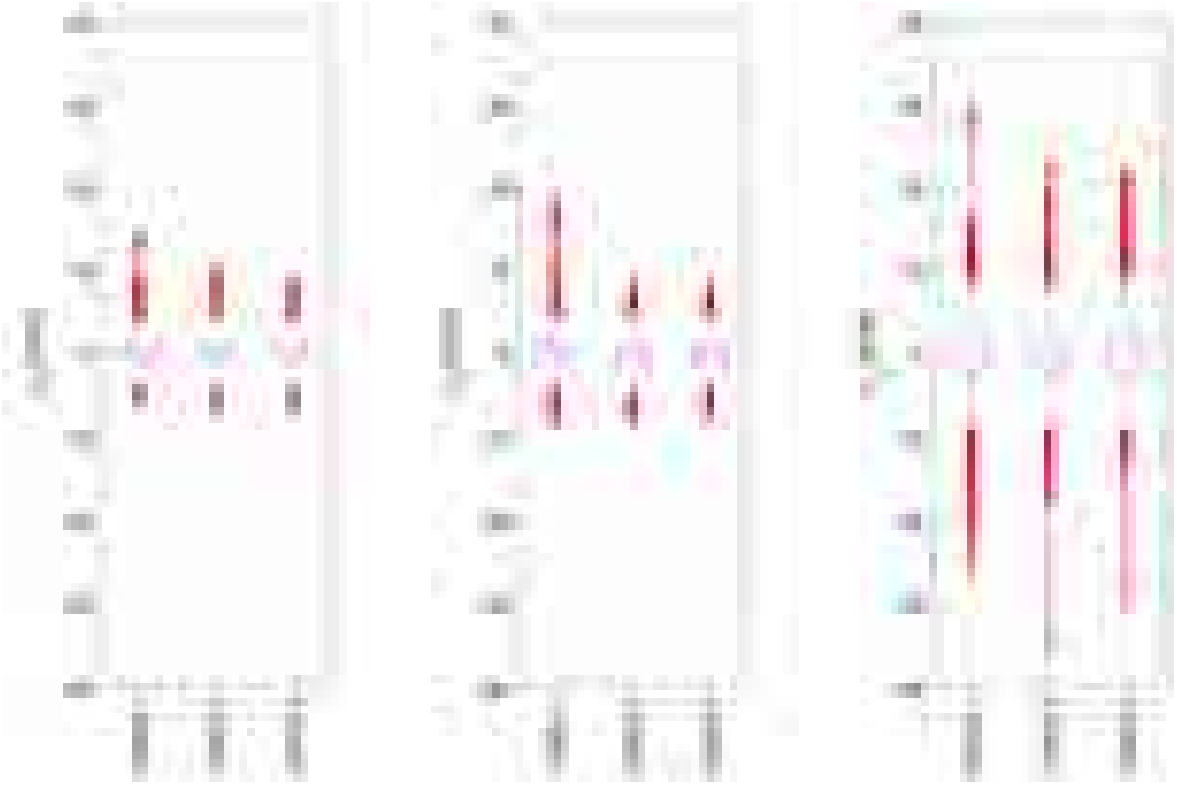

Figure 39. Comparison of the boxplots.

Table 7. Comparison of the results obtain for analysis of displacements in x direction.

Receiver [-]	**Mean** [mm]	**Var** [mm^2]	**Std** [mm]	**Perc. 99.95 %** [mm]	**Perc. 0.05 %** [mm]	**Threshold** [mm]
GNSS 1	-0.03	2.41	1.55	4.72	-3.98	4.35
GNSS 2	0.06	2.87	1.70	5.04	-4.32	4.68
GNSS 3	-0.01	2.59	1.61	4.76	-4.09	4.43
Average	0.01	2.62	1.62	4.84	-4.13	4.49

Table 8. Comparison of the results obtain for analysis of displacements in y direction.

Receiver [-]	**Mean** [mm]	**Var** [mm^2]	**Std** [mm]	**Perc. 99.95 %** [mm]	**Perc. 0.05 %** [mm]	**Threshold** [mm]
GNSS 1	0.09	3.05	1.75	4.98	-4.59	4.79
GNSS 2	-0.09	3.29	1.81	4.96	-4.89	4.93
GNSS 3	0.09	2.91	1.71	4.76	-4.35	4.56
Average	0.03	3.08	1.76	4.9	-4.61	4.76

Table 9. Comparison of the results obtain for analysis of displacements in z direction.

Receiver [-]	**Mean** [mm]	**Var** [mm^2]	**Std** [mm]	**Perc. 99.95 %** [mm]	**Perc. 0.05 %** [mm]	**Threshold** [mm]
GNSS 1	-0.07	11.37	3.37	8.97	-8.83	8.90
GNSS 2	-0.17	11.06	3.33	9.26	-8.27	8.77
GNSS 3	-0.04	12.36	3.52	9.65	-9.11	9.38
Average	-0.09	11.60	3.41	9.29	-8.74	9.02

In conclusion, the vertical and horizontal minimal sensible displacements are 9 mm and 5 mm, approximately, the latter was calculated as the average between the results obtained from the analysis of the x and y displacements. As it can be noticed, the minimal sensible displacements in both direction is almost double compared to the results obtained in the test. This may be due to the signal's disturbances produced by the passage of the vehicles.

7 Results

The results of the monitoring campaign are presented in the following paragraphs. First, the comparative analysis between the accelerometric and the GNSS monitoring system are shown. Since the only accelerometer adopted was installed on point number 2 (refer to Figure 26), the comparison was carried out with GNSS2. Due to the different nature of the structure compared to the one monitored in the test, the comparison was carried out only in the time domain. Indeed, the test of the monitoring system consisted of acquiring in continuous the position of three points of the road bridge under normal traffic condition. The source of excitation is represented by the vehicles that cross the road bridge. By analyzing the signal in the time domain, we can notice that the crossing of the vehicles generates a very short in time displacement. The amplitude of the displacement depends on the weight of the vehicles. It is important to let the reader notice that due to the rigid nature of the structure, the free oscillations cannot be discerned from the signal. As an example, in Figure 40 and Figure 41 the accelerometric signals acquired in the test and the validation, respectively, are shown. In the test, the type of structure monitored and excitation performed made it possible to acquire a signal in which the forced and free oscillations can be clearly recognized, as highlighted in Figure 40. On the other hand, in the validation, the acquired signal shows very short in time displacements in which the forced and free oscillations cannot be recognized, as shown in Figure 41. The methodology applied in the test could not have been applied to the present case in order to evaluate the natural frequencies of the structure.

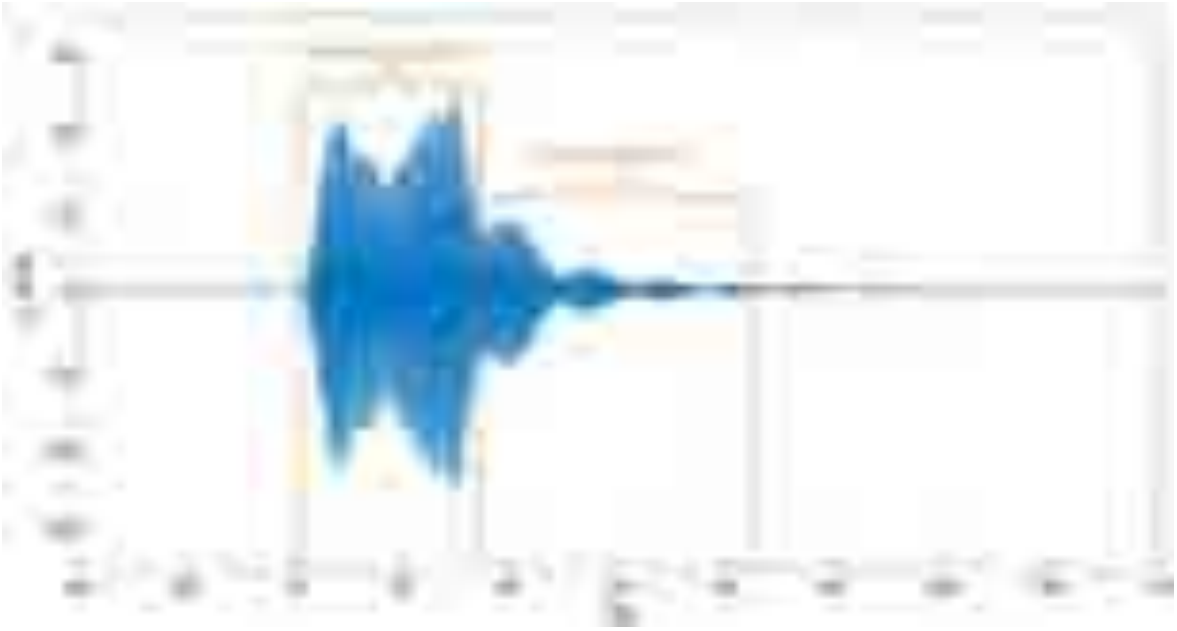

Figure 40. Generic accelerometric signal acquired in the test in which the ranges of free and forced oscillations are highlighted.

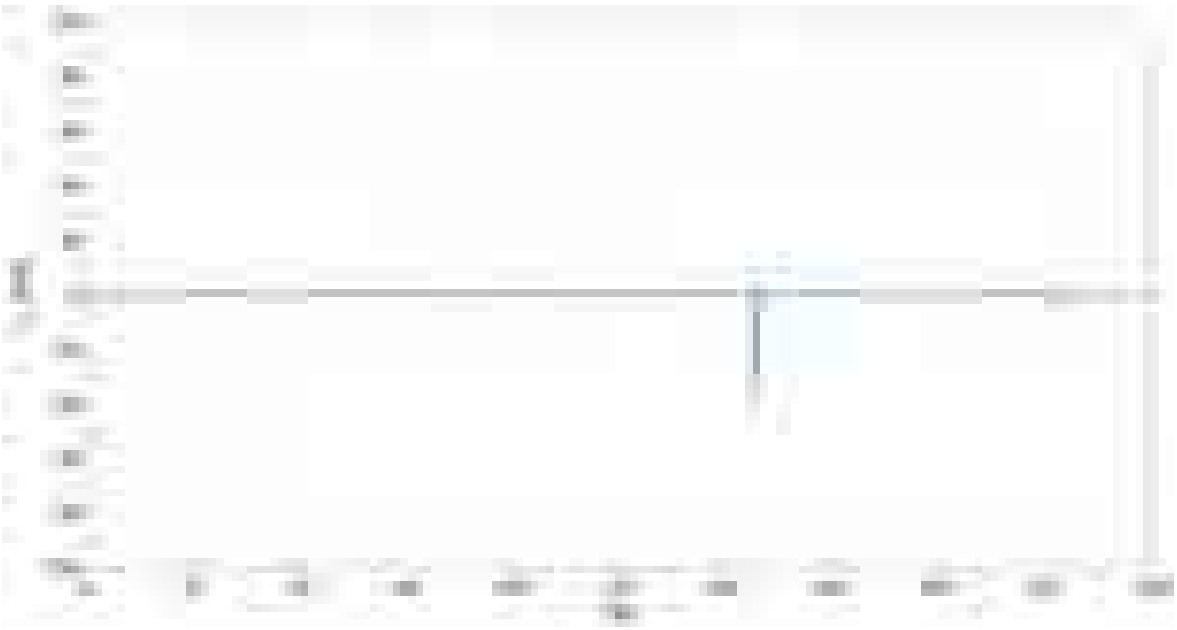

Figure 41. Generic accelerometric signal acquired in the validation.

Moreover, the GNSS signal appears to be very noisy, as shown in Figure 42. Indeed, as reported in the previous statistical analysis, the minimum threshold of the vertical displacements resulted to be approximately 10mm. Even in case of an artificial performed

excitation that could generate not so short in time displacements, the free oscillations would reasonably get lost in the noise of the signal.

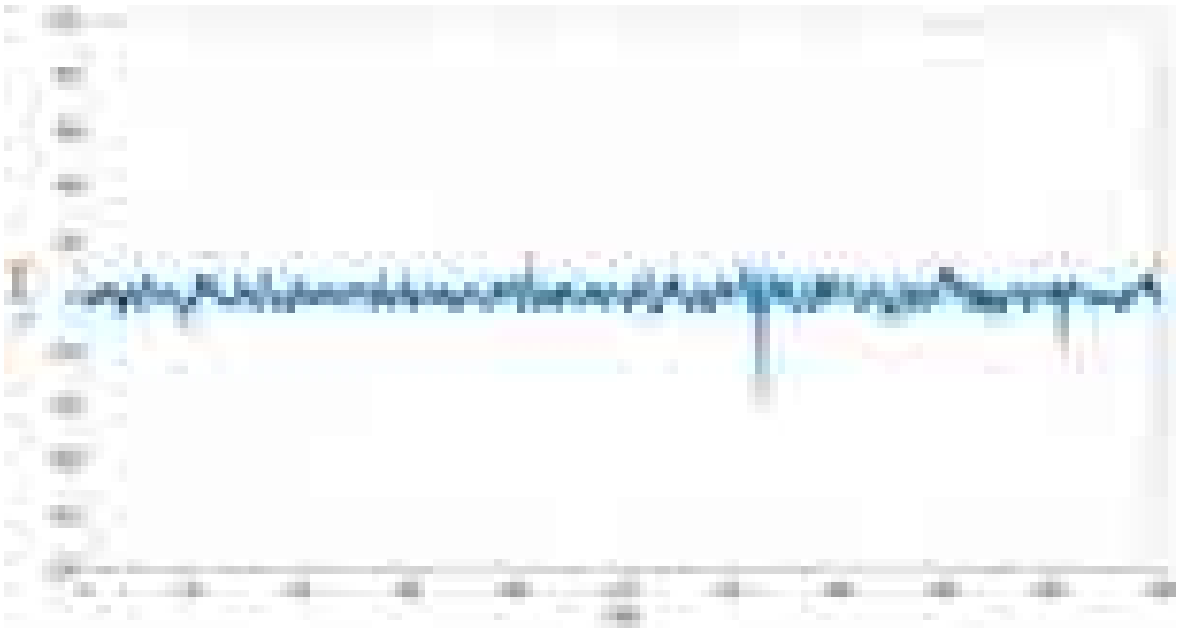

Figure 42. Generic GNSS signal acquired in the validation.

In the following paragraph, the comparative analysis between the satellite signal (GNSS2) and the accelerometric signal is presented. Moreover, the results acquired by the three GNSS receivers are compared in a series of subplots in order to show the potential of the GNSS system when installed in different points of the structure.

7.1 Comparative analysis

A series of graphical analysis carried out on the acquisitions made during the monitoring campaign are presented from Figure 43 to Figure 48. The analysis involves the 1-hour interval data that was acquired during the 21st of September 2021, starting at 6:37 am, and those acquired during the 24th, starting at 1:26 am and 8:26 am, respectively. Therefore, on the x-axis the time is reported in seconds, going form 0 s to 3600 s. To highlight the result, in the following figures some captions of those acquisitions are presented, highlighting the displacements peaks that were acquired by both the monitoring systems. On the y-axis the displacements of the bridge along the vertical direction are reported in millimeters. Each figure shows two subplots, the one above refers to the GNSS signal while

the one below the accelerometric signal. Among the various acquisitions those are the only ones in which a clear correspondence between GNSS and accelerometric system could be appreciated. Due to the threshold of the minimal sensible displacement (refer to the statistical analysis previously conducted), the only peaks that could be acquired by means of the GNSS system were those higher than 10 mm, approximately. As an example, Figure 43 shows a peak of about 18mm that was acquired by the accelerometric system. The peak is quite higher than the minimal sensible displacement of the GNSS system, hence, in this case, the satellite system manages to capture the peak, showing just a slight difference of about 2mm.

Figure 43. First analysis of the acquisition of the 21st September 2021, started at 6:37:50 am: (above) GNSS signal; (below) accelerometric signal.

Instead, when the peak has an amplitude similar to the minimal sensible displacement, the GNSS struggles to identify it. This happens for example in Figure 44, where the peak identified by the accelerometric system is about 12mm. In this case, the GNSS managed to identify the correct peak but the difference with the amplitude identified by the accelerometer is much larger.

Figure 44. Second analysis of the acquisition of the 21st September 2021, started at 6:37:50 am: (above) GNSS signal; (below) accelerometric signal.

Figure 45. Analysis of the acquisition of the 24th September 2021, started at 1:26:22 am: (above) GNSS signal; (below) accelerometric signal.

Figure 46. First analysis of the acquisition of the 24th September 2021, started at 8:26:28 am: (above) GNSS signal; (below) accelerometric signal.

Figure 47.Second analysis of the acquisition of the 24th September 2021, started at 8:26:28 am: (above) GNSS signal; (below) accelerometric signal.

Figure 48. Third analysis of the acquisition of the 24th September 2021, started at 8:26:28 am: (above) GNSS signal; (below) accelerometric signal.

In conclusion, the GNSS managed to identify the peak displacements that are reasonably due to the crossing of heavy vehicles. Indeed, as it can be seen from the accelerometric signals depicted before, there are some small peaks, that cannot be identified by the GNSS since they get lost in the noise. The only peaks that could be identified through the analysis of the GNSS signal were those higher than the minimal sensible displacement of the system, which appears to be about 10 mm, as reported in the results of the statistical analysis. Hence, the smaller the peak, the higher will be the error in the identification through GNSS, as it can be observed by the results that are summed up in Table 10. In the table, the column "Time" shows the time when the peak was registered by the two monitoring systems, expressed in seconds from the starting of the acquisition ("Starting UTC time"). The column "Displacement" shows the amplitude of the peaks registered by the two monitoring systems, expressed in mm.

Table 10. Results of the comparative analysis.

Interval	Date	Starting UTC time	Time		Displacement			
			GNSS	Acc.	GNSS	Acc.	Diff.	Diff.
[-]	[-]	[-]	[s]	[s]	[mm]	[mm]	[mm]	[%]
1	21/09/2021	6:37:50 am	39	39	16	18	2	11
2	21/09/2021	6:37:50 am	938	938	20	12	8	40
3	24/09/2021	1:26:22 am	315	315	36	38	2	5
4	24/09/2021	8:26:28 am	794	794	40	37	3	8
5	24/09/2021	8:26:28 am	2664	2663	17	11	6	35
6	24/09/2021	8:26:28 am	3373	3372	17	5	12	71
						Average	5.5	28

7.2 GNSS results

The comparison of the three GNSS receivers is presented from Figure 49 to Figure 51. The comparison is carried out only on the signals acquired during the 24th of September 2021, since on the 21st only GNSS 2 was acquiring. The same time intervals shown before are here depicted for all three GNSS receivers. The acquisitions refer to the time intervals that started at 1:26 am and 8:26 am. The only time interval left out is number 6 (refer to the previous table) in which GNSS 1 and GNSS 3 did not manage to acquire anything, due to the fact that the peak displacement in this case was very small.

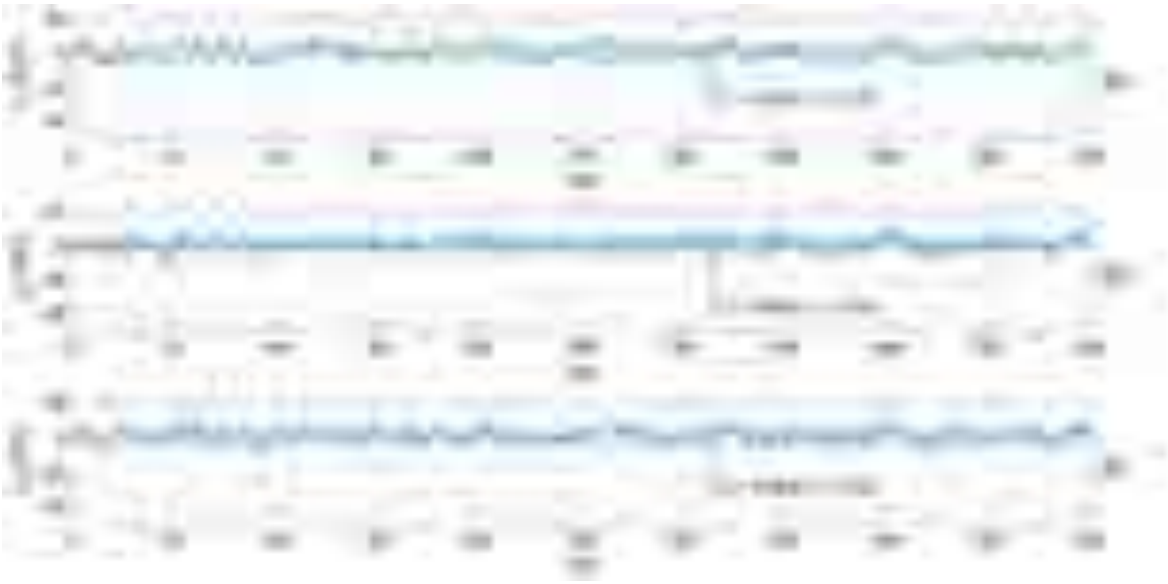

Figure 49. GNSS acquisitions of the 24th September 2021, started at 8:26:28 am: (a) GNSS 1; (b) GNSS 2; (c) GNSS 3.

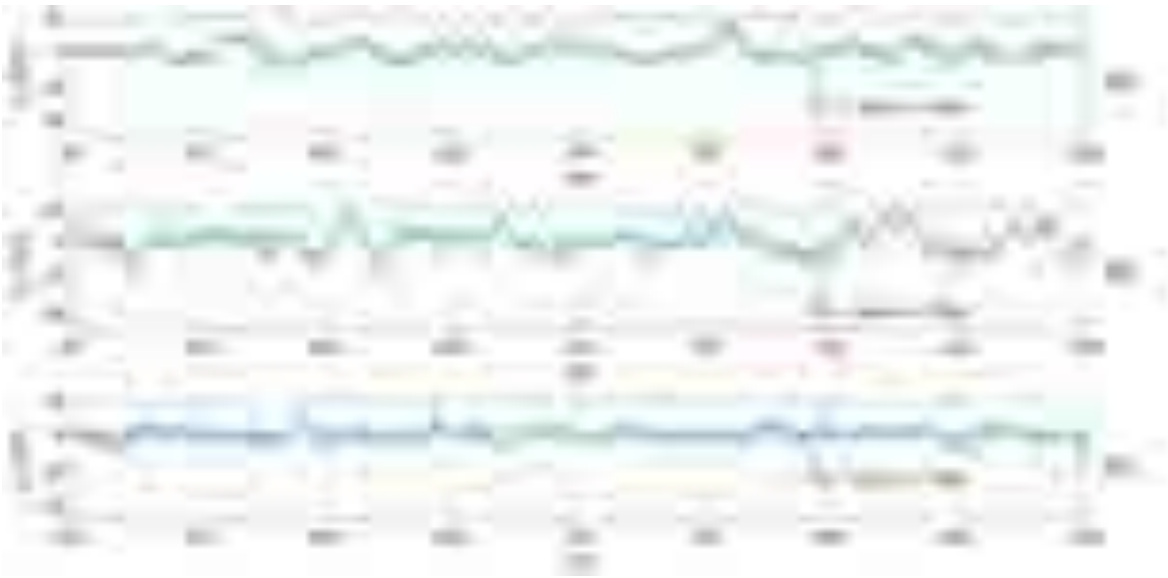

Figure 50. First GNSS acquisitions of the 24th September 2021, started at 8:26:28 am: (a) GNSS 1; (b) GNSS 2; (c) GNSS 3.

Figure 51. Second GNSS acquisitions of the 24th September 2021, started at 8:26:28 am: (a) GNSS 1; (b) GNSS 2; (c) GNSS 3.

As it can be noticed, the GNSS receivers always managed to acquire the peak. The amplitude of the displacement depends on which point of the structure was being monitored and this is why the three GNSS receivers gave different results in terms of peak's amplitude. In Table 11 the comparison of the results acquired by the three GNSS receivers is presented.

Table 11. Results of the three GNSS receivers.

Interval	**Date**	**Starting UTC time**	**Time**			**Displacement**		
			GNSS 1	**GNSS 2**	**GNSS 3**	**GNSS 1**	**GNSS 2**	**GNSS 3**
[-]	[-]	[-]	[s]	[s]	[s]	[mm]	[mm]	[mm]
3	24/09/2021	1:26:22 am	315	315	315	26	36	29
4	24/09/2021	8:26:28 am	794	794	793	33	40	27
5	24/09/2021	8:26:28 am	2664	2664	2665	13	17	37

8 Conclusion

The test carried out in the validation consisted of monitoring a road bridge through the GNSS system. The performance of the system was already tested during the test on a benchmark structure, through a comparative analysis in the time and frequency domain by means of an accelerometric system. For the new test, the accuracy of the system when installed on a structure of civil interest was investigated. For this purpose, a road bridge located in the north of Rome was chosen as a real case scenario to monitor under normal traffic conditions. The results of the monitoring campaign were analyzed in order to define the minimal sensible displacement and the accuracy of the system. The same methodology of the test was adopted to evaluate the minimal sensible displacement, which consisted of a statistical analysis carried out on the noise of the GNSS signal. The results showed that the vertical and horizontal minimal sensible displacements are about 9mm and 5mm respectively. Compared to the results of the test, in which an ideal scenario without disturbances was study, the minimal sensible displacements seem to double. Indeed, in the case of the road bridge, it must be taken into consideration that the crossing of the vehicles, close to the installation points of the GNSS sensors, inevitably affect the acquisition of the satellite signal. Nevertheless, the minimal sensible displacements showed again a relatively small value (smaller than the cm scale). Those values are suitable for monitoring slender metallic structure and more in general very flexible structures; tall buildings under wind excitation; slender bridges and for buildings in case of events like medium earthquakes, when the order of magnitude of displacements overcome the values aforementioned.

The same methodology of the test was adopted to evaluate the accuracy, consisting of the comparative analysis with the results of the accelerometric system. As already explained in the previous paragraph, due to difficulties encountered in detecting the free oscillations of the structure from the acquired GNSS signal, it was not possible to carry out a comparative analysis in the frequency domain through the methodology herein adopted. Therefore, the accuracy was investigated by means of a comparative analysis in the time domain. All the GNSS sensors managed to identify those peak displacements that were bigger than the minimal sensible displacements, reasonably caused by the crossing of heavy vehicles. Due

to the structure being old and in need of restoration, ANAS s.p.a., the company that manages the infrastructure, imposed a partial stop to heavy traffic in order to prevent risks to the structure and to the users of the infrastructure. Therefore, the monitoring carried out with these traffic conditions did not lead to many peak displacements that could be registered by the GNSS system. The comparison showed an average difference of about 5mm, the same order of magnitude obtained in the test. The events captured by both systems are perfectly synchronized, showing again that the GNSS system is capable of acquiring the dynamic behavior of the structure. The amplitude of the peak displacements depends on both the excitation applied to the structure and its stiffness. Hence, this could be further used as indicator for traffic control or structural safety.

9 Annex

9.1 Results of the statistical analysis during the test

9.1.1 GNSS 1

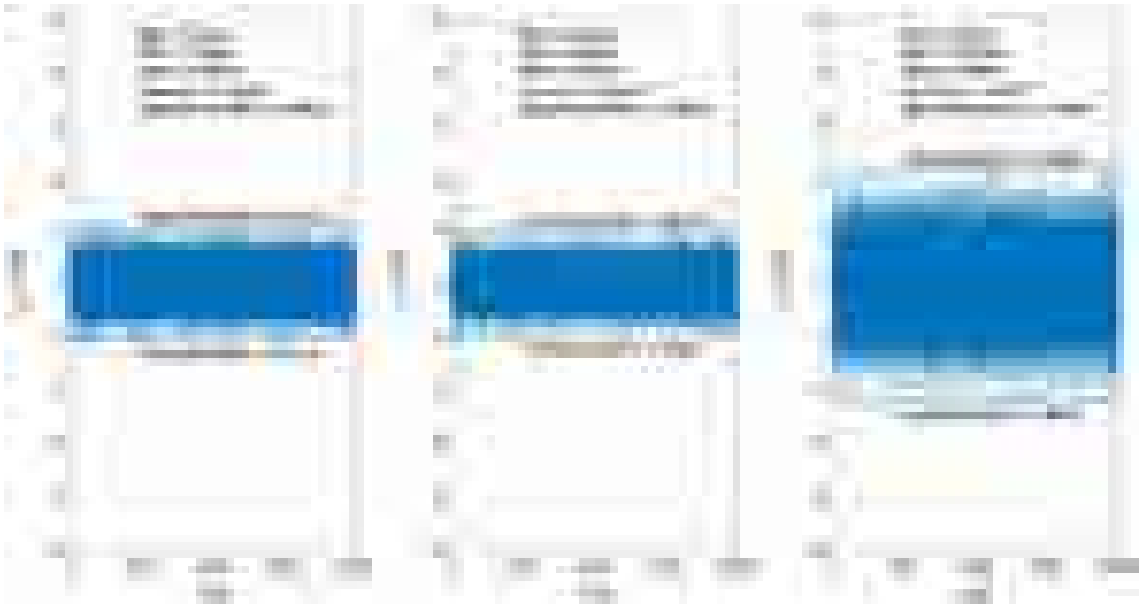

Figure 52. Signals of GNSS 1 for the x, y and z displacements.

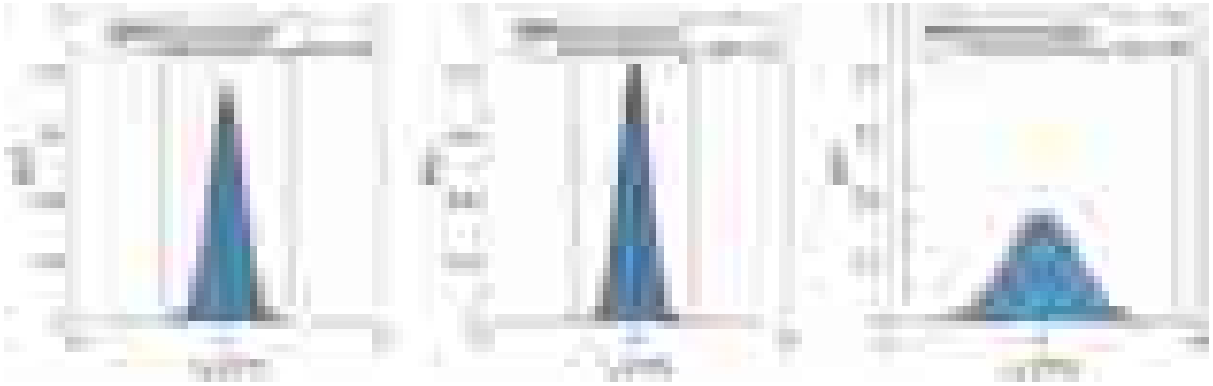

Figure 53. Normal distributions of the noise of GNSS 1.

Figure 54. Position of GNSS 1 in local reference system.

Table 12. Results of statistical analysis on GNSS 1.

	max	min	mean	variance	Standard deviation	Percentile 99.95 %	Percentile 0.05 %	Threshold
	[mm]	[mm]	[mm]	[mm²]	[mm]	[mm]	[mm]	[mm]
x	4.41	-7.20	0.00	0.30	0.55	2.11	-2.11	2.11
y	4.07	-6.35	0.00	0.24	0.48	1.94	-1.92	1.93
z	7.30	-12.45	0.00	1.35	1.16	4.28	-4.40	4.34

9.1.2 GNSS 2

Figure 55. Signals of GNSS 2 for the x, y and z displacements.

Figure 56. Normal distributions of the noise of GNSS 2.

Figure 57. Position of GNSS 2 in local reference system.

Table 13. Results of statistical analysis on GNSS 2.

	max	**min**	**mean**	**variance**	**Standard deviation**	**Percentile 99.95 %**	**Percentile 0.05 %**	**Threshold**
	[mm]	[mm]	[mm]	[mm^2]	[mm]	[mm]	[mm]	[mm]
x	4.07	-4.47	0.00	0.34	0.59	2.30	-2.17	2.24
y	4.01	-2.32	0.00	0.24	0.49	1.87	-1.79	1.83
z	5.89	-8.23	0.00	1.40	1.18	4.53	-4.55	4.54

9.1.3 GNSS 3

Figure 58. Signals of GNSS 3 for the x, y and z displacements.

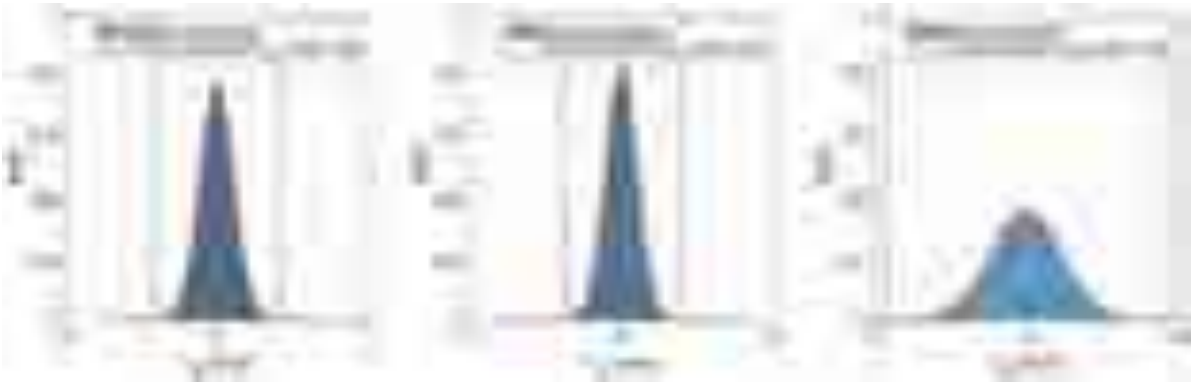

Figure 59. Normal distributions of the noise of GNSS 3.

Figure 60. Position of GNSS 3 in local reference system.

Table 14. Results of statistical analysis on GNSS 3.

	max	min	mean	variance	Standard deviation	Percentile 99.95 %	Percentile 0.05 %	Threshold
	[mm]	[mm]	[mm]	[mm²]	[mm]	[mm]	[mm]	[mm]
x	3.50	-3.33	0.00	0.29	0.54	2.11	-2.04	2.08
y	4.08	-3.95	0.00	0.25	0.50	1.94	-1.87	1.91
z	10.50	-10.33	0.00	1.35	1.16	4.63	-4.54	4.59

9.1.4 GNSS 4

Figure 61. Signals of GNSS 4 for the x, y and z displacements.

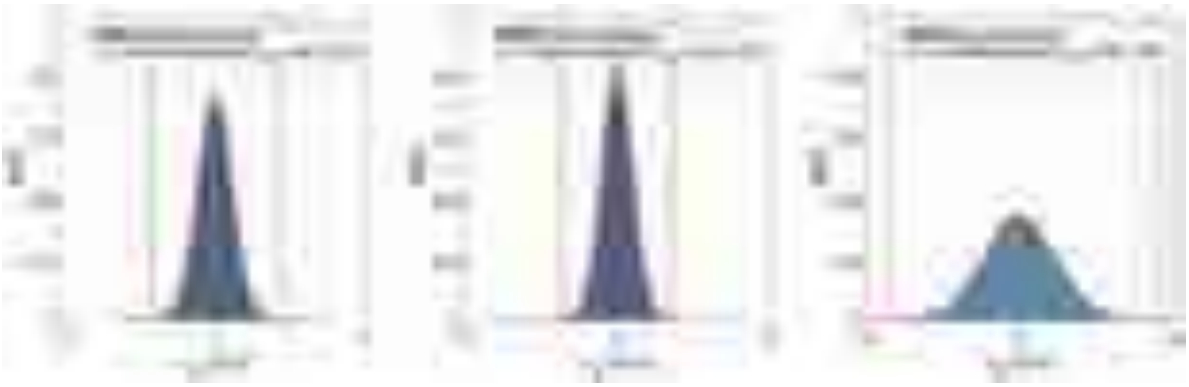

Figure 62. Normal distributions of the noise of GNSS 4.

Figure 63. Position of GNSS 4 in local reference system.

Table 15. Results of statistical analysis on GNSS 4.

	max	**min**	**mean**	**variance**	**Standard deviation**	**Percentile 99.95 %**	**Percentile 0.05 %**	**Threshold**
	[mm]	[mm]	[mm]	[mm^2]	[mm]	[mm]	[mm]	[mm]
x	3.29	-3.12	0.00	0.31	0.56	2.14	-2.10	2.12
y	2.85	-3.40	0.00	0.25	0.50	1.81	-1.83	1.82
z	6.03	-6.88	0.00	1.41	1.19	4.54	-4.35	4.45

9.1.5 GNSS 5

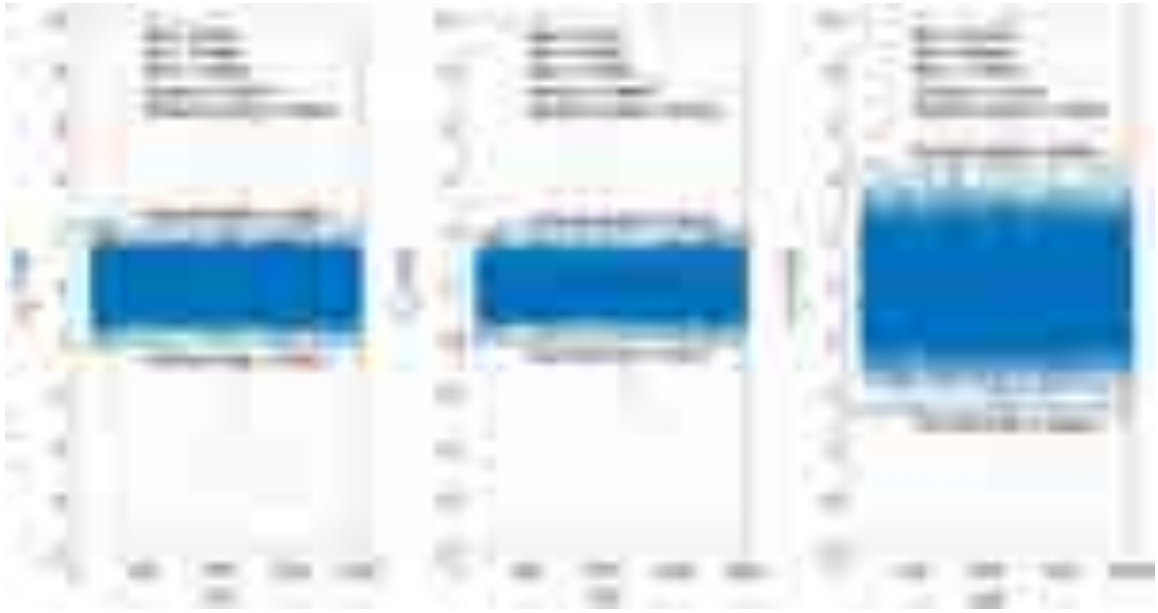

Figure 64. Signals of GNSS 5 for the x, y and z displacements.

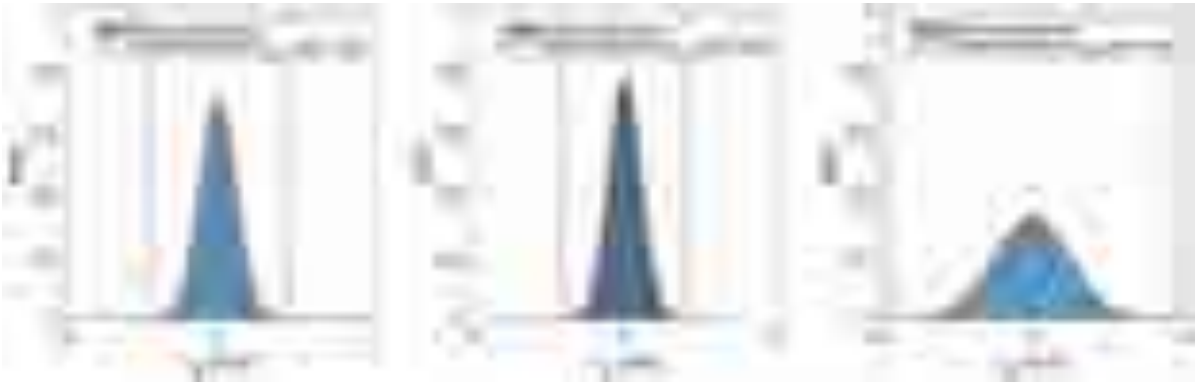

Figure 65. Normal distributions of the noise of GNSS 5.

Figure 66. Position of GNSS 5 in local reference system.

Table 16. Results of statistical analysis on GNSS 5.

	max	**min**	**mean**	**variance**	**Standard deviation**	**Percentile 99.95 %**	**Percentile 0.05 %**	**Threshold**
	[mm]	[mm]	[mm]	[mm²]	[mm]	[mm]	[mm]	[mm]
x	5.63	-9.19	0.00	0.34	0.59	2.24	-2.25	2.25
y	3.21	-3.75	0.00	0.28	0.53	1.99	-2.05	2.02
z	13.07	-6.85	0.00	1.51	1.23	4.56	-4.63	4.60

9.1.6 Comparison of the GNSS receivers

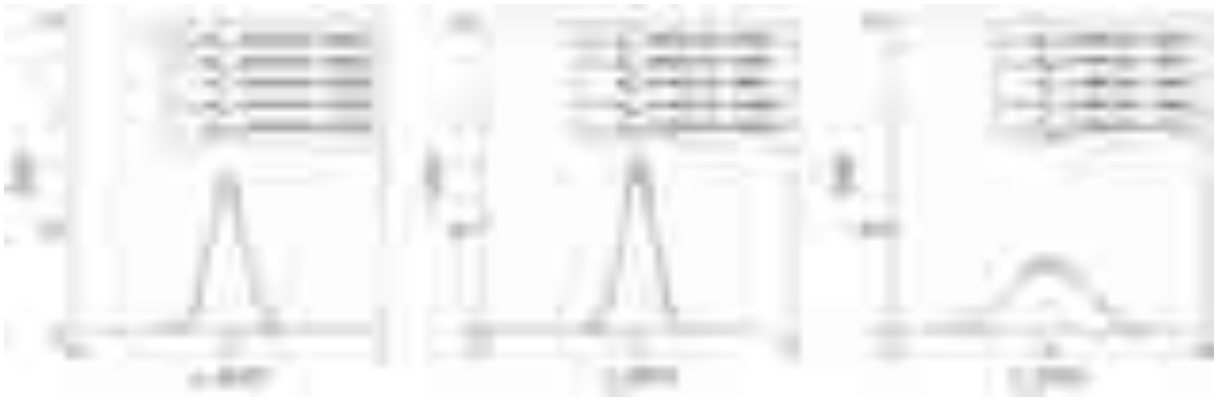

Figure 67. Normal distributions comparison.

Table 17. Comparison of the results obtain for analysis of displacements in x direction.

	max	**min**	**mean**	**variance**	**Standard deviation**	**Percentile 99.95 %**	**Percentile 0.05 %**	**Threshold**
	[mm]	[mm]	[mm]	[mm^2]	[mm]	[mm]	[mm]	[mm]
GNSS 1	4.41	-7.20	0.00	0.30	0.55	2.11	-2.11	2.11
GNSS 2	4.07	-4.47	0.00	0.34	0.59	2.30	-2.17	2.24
GNSS 3	3.50	-3.33	0.00	0.29	0.54	2.11	-2.04	2.08
GNSS 4	3.29	-3.12	0.00	0.31	0.56	2.14	-2.10	2.12
GNSS 5	5.63	-9.19	0.00	0.34	0.59	2.24	-2.25	2.25
mean	4.18	-5.46	0.00	0.32	0.57	2.18	-2.13	2.16

Table 18. Comparison of the results obtain for analysis of displacements in y direction.

	max	**min**	**mean**	**variance**	**Standard deviation**	**Percentile 99.95 %**	**Percentile 0.05 %**	**Threshold**
	[mm]	[mm]	[mm]	[mm^2]	[mm]	[mm]	[mm]	[mm]
GNSS 1	4.07	-6.35	0.00	0.24	0.48	1.94	-1.92	1.93
GNSS 2	4.01	-2.32	0.00	0.24	0.49	1.87	-1.79	1.83
GNSS 3	4.08	-3.95	0.00	0.25	0.50	1.94	-1.87	1.91
GNSS 4	2.85	-3.40	0.00	0.25	0.50	1.81	-1.83	1.82
GNSS 5	3.21	-3.75	0.00	0.28	0.53	1.99	-2.05	2.02
mean	3.64	-3.95	0.00	0.25	0.50	1.91	-1.89	1.9

Table 19. Comparison of the results obtain for analysis of displacements in z direction.

	max	**min**	**mean**	**variance**	**Standard deviation**	**Percentile 99.95 %**	**Percentile 0.05 %**	**Threshold**
	[mm]	[mm]	[mm]	[mm^2]	[mm]	[mm]	[mm]	[mm]
GNSS 1	7.30	-12.45	0.00	1.35	1.16	4.28	-4.40	4.34
GNSS 2	5.89	-8.23	0.00	1.40	1.18	4.53	-4.55	4.54
GNSS 3	10.50	-10.33	0.00	1.35	1.16	4.63	-4.54	4.59
GNSS 4	6.03	-6.88	0.00	1.41	1.19	4.54	-4.35	4.45
GNSS 5	13.07	-6.85	0.00	1.51	1.23	4.56	-4.63	4.60
mean	8.56	-8.95	0.00	1.40	1.18	4.51	-4.49	4.50

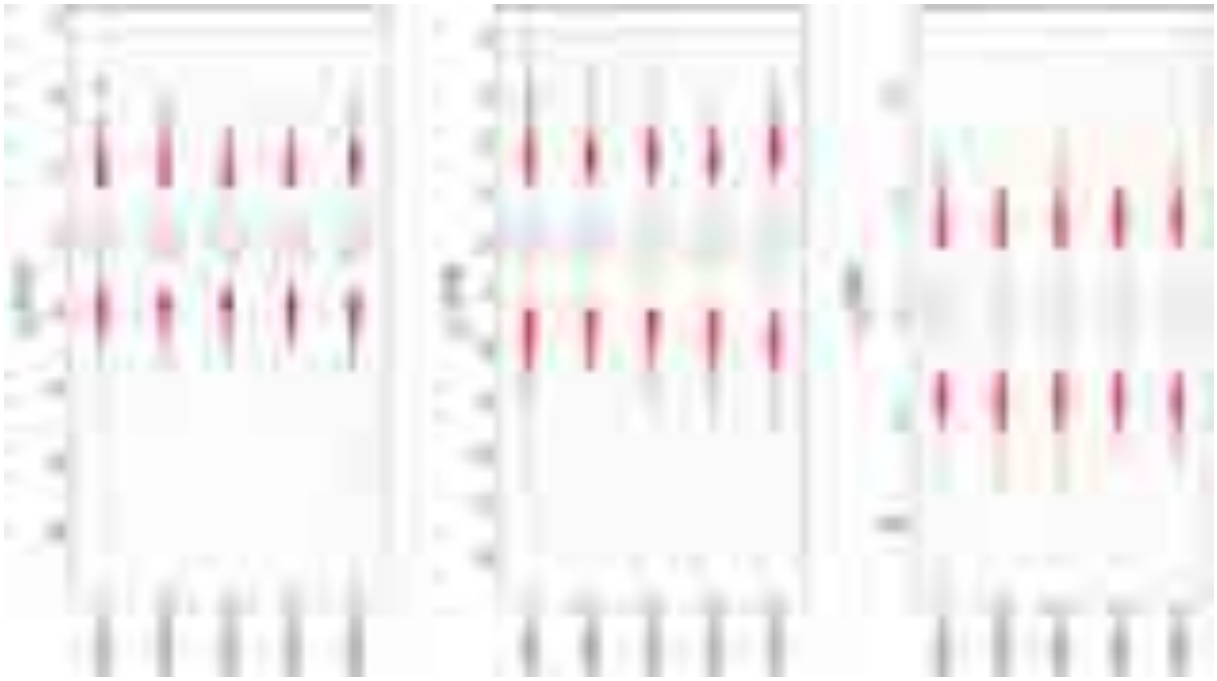

Figure 68. Boxplots comparison.

In conclusion, the vertical and horizontal minimal sensible displacements are 4.50 mm and 2.03 mm respectively, the latter was calculated as the average between the results obtained from the analysis of the x and y displacements.

9.2 Results of the test in the time domain

9.2.1 Test 2

Figure 69. Comparison in the time domain between the GNSS (above) and accelerometric (below) signals of point monitored 1 acquired in test 2 during the test.

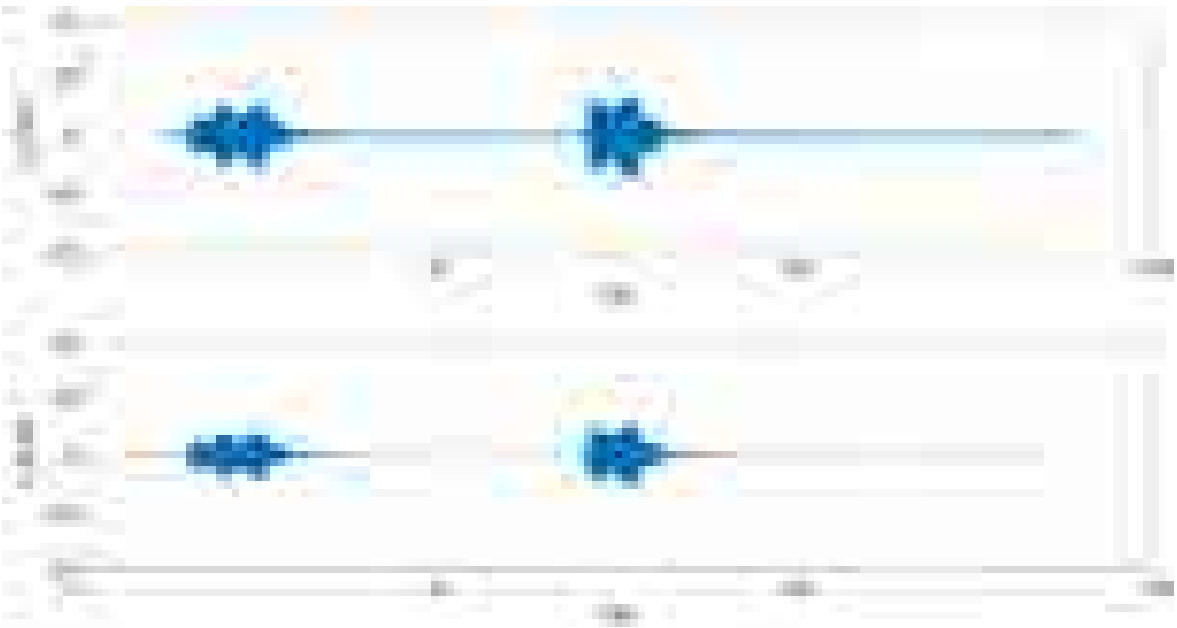

Figure 70. Comparison in the time domain between the GNSS (above) and accelerometric (below) signals of point monitored 2 acquired in test 2 during the test.

Figure 71. Comparison in the time domain between the GNSS (above) and accelerometric (below) signals of point monitored 3 acquired in test 2 during the test.

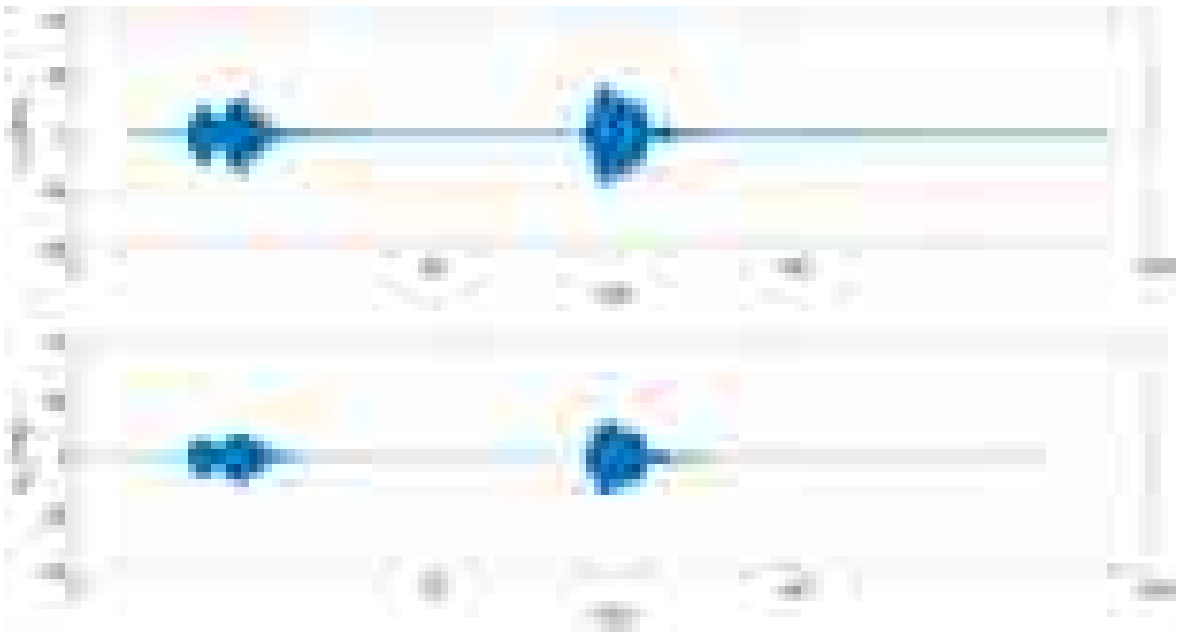

Figure 72. Comparison in the time domain between the GNSS (above) and accelerometric (below) signals of point monitored 4 acquired in test 2 during the test.

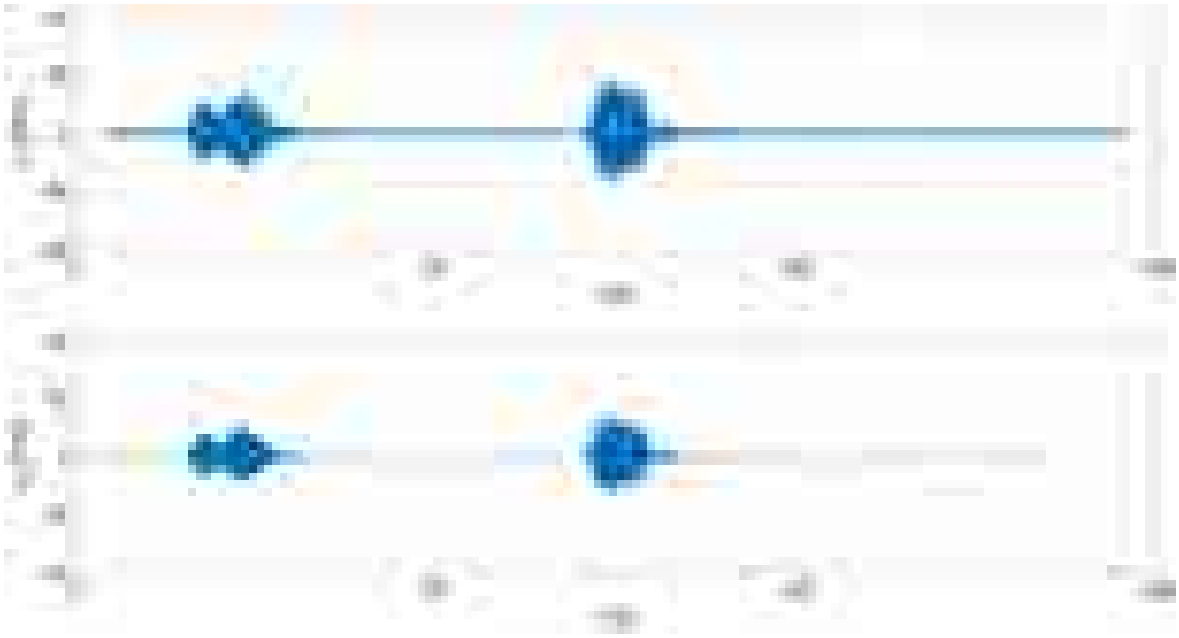

Figure 73. Comparison in the time domain between the GNSS (above) and accelerometric (below) signals of point monitored 5 acquired in test 2 during the test.

Table 20. Results in the time domain of test 2 during the test.

Point	Displacement 1				Displacement 2			
	GNSS	Acc.	Diff.	Diff.	GNSS	Acc.	Diff.	Diff.
[-]	[mm]	[mm]	[mm]	[%]	[mm]	[mm]	[mm]	[%]
1	25.4	18.7	6.7	26.4	31.6	24.9	6.7	21.2
2	12.6	8.9	3.7	29.4	15.4	11.4	4.0	26.0
3	5.8	3.4	2.4	41.4	7.3	4.7	2.6	35.6
4	12.8	9.1	3.7	28.9	17.6	12.7	4.9	27.8
5	14.6	9.9	4.7	32.2	18.0	13.2	4.8	26.7
Average			4.2	31.7			4.6	27.5
Average (without point 3)			4.7	29.2			5.1	25.4

9.2.2 Test 3

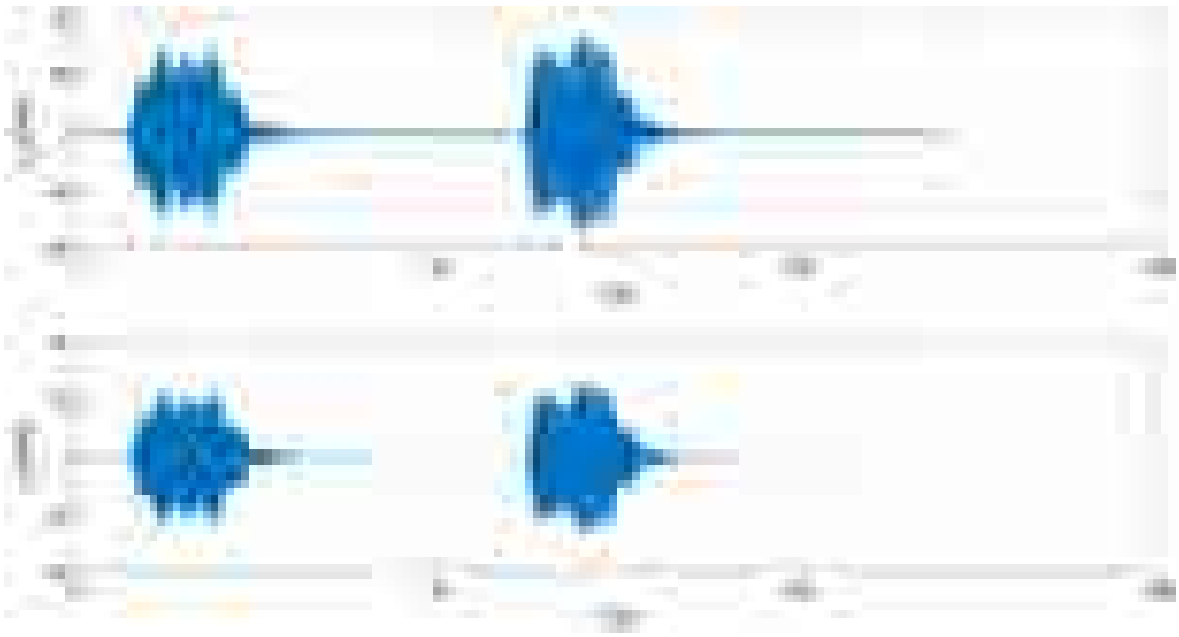

Figure 74. Comparison in the time domain between the GNSS (above) and accelerometric (below) signals of point monitored 1 acquired in test 3 during the test.

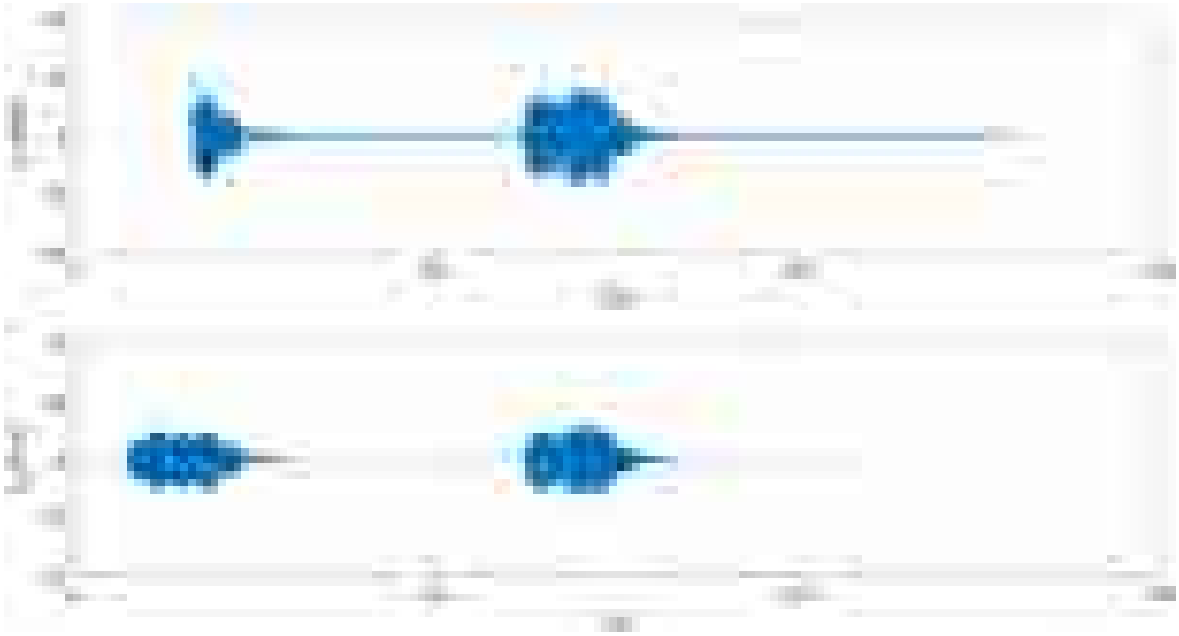

Figure 75. Comparison in the time domain between the GNSS (above) and accelerometric (below) signals of point monitored 2 acquired in test 3 during the test.

Figure 76. Comparison in the time domain between the GNSS (above) and accelerometric (below) signals of point monitored 3 acquired in test 3 during the test.

Figure 77. Comparison in the time domain between the GNSS (above) and accelerometric (below) signals of point monitored 4 acquired in test 3 during the test.

Figure 78. Comparison in the time domain between the GNSS (above) and accelerometric (below) signals of point monitored 5 acquired in test 3 during the test.

Table 21. Results in the time domain of test 3 during the test.

Point	Displacement 1				Displacement 2			
	GNSS	Acc.	Diff.	Diff.	GNSS	Acc.	Diff.	Diff.
[-]	[mm]	[mm]	[mm]	[%]	[mm]	[mm]	[mm]	[%]
1	31.2	24.7	6.5	20.8	34.8	26.1	8.7	25.0
2	14.5	11.0	3.5	24.1	17.2	12.1	5.1	29.7
3	9.2	5.4	3.8	41.3	11.6	7.6	4.0	34.5
4	20.0	14.4	5.6	28.0	25.2	18.2	7.0	27.8
5	20.6	15.6	5.0	24.3	25.7	17.5	8.2	31.9
Average			4.9	27.7			6.6	29.8
Average (without point 3)			5.2	24.3			7.3	28.6

9.2.3 Test 4

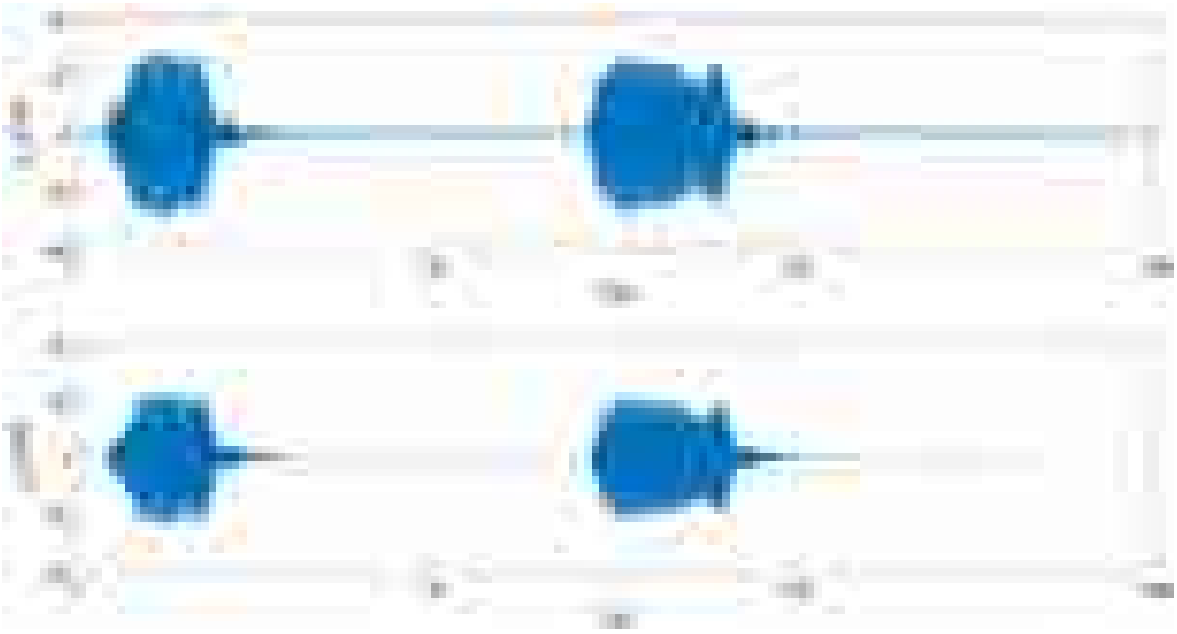

Figure 79. Comparison in the time domain between the GNSS (above) and accelerometric (below) signals of point monitored 1 acquired in test 4 during the test.

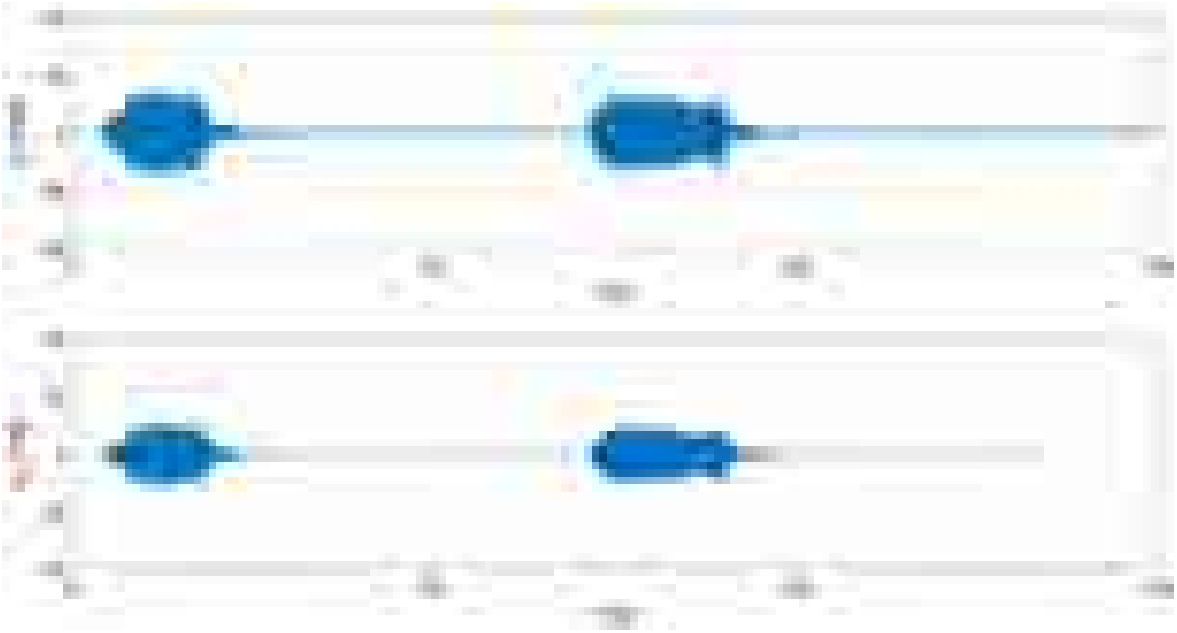

Figure 80. Comparison in the time domain between the GNSS (above) and accelerometric (below) signals of point monitored 2 acquired in test 4 during the test.

Figure 81. Comparison in the time domain between the GNSS (above) and accelerometric (below) signals of point monitored 3 acquired in test 4 during the test.

Figure 82. Comparison in the time domain between the GNSS (above) and accelerometric (below) signals of point monitored 4 acquired in test 4 during the test.

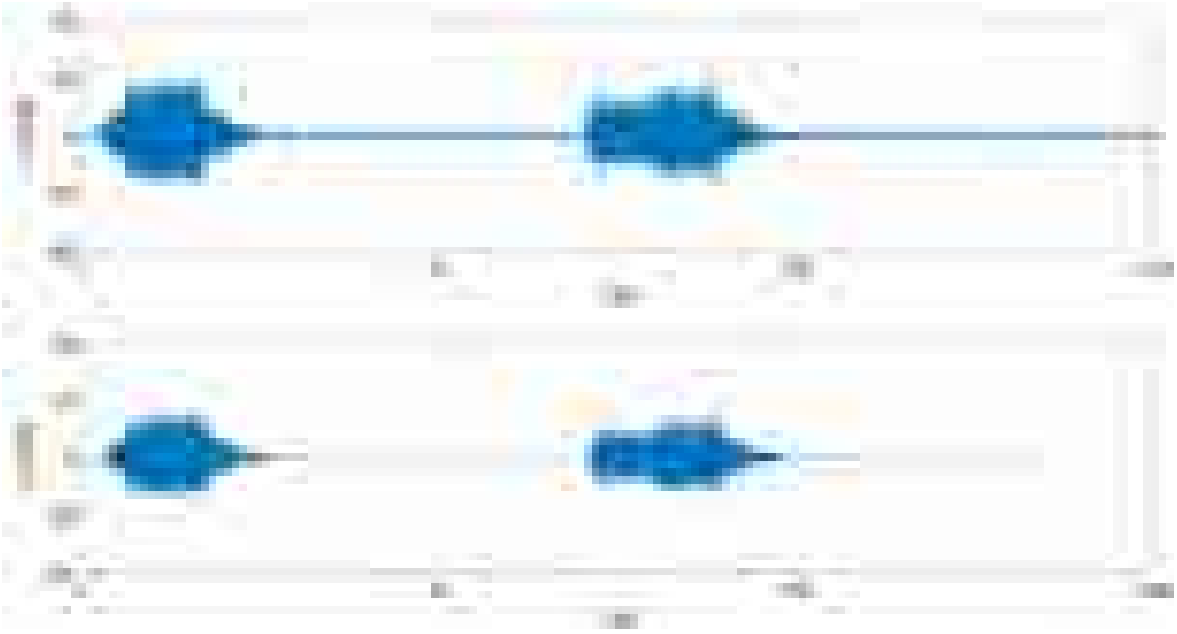

Figure 83. Comparison in the time domain between the GNSS (above) and accelerometric (below) signals of point monitored 5 acquired in test 4 during the test.

Table 22. Results in the time domain of test 4 during the test.

Point	Displacement 1				Displacement 2			
	GNSS	Acc.	Diff.	Diff.	GNSS	Acc.	Diff.	Diff.
[-]	[mm]	[mm]	[mm]	[%]	[mm]	[mm]	[mm]	[%]
1	28.3	22.9	5.4	19.1	28.6	21.5	7.1	24.8
2	14.9	10.7	4.2	28.2	13.3	10.1	3.2	24.1
3	10.5	7.2	3.3	31.4	9.8	6.6	3.2	32.7
4	22.6	16.3	6.3	27.9	19.0	15.1	3.9	20.5
5	20.0	16.4	3.6	18.0	19.1	15.4	3.7	19.4
Average			4.6	24.9			4.2	24.3
Average (without point 3)			4.9	23.3			4.5	22.2

9.3 Results of the test in the frequency domain

9.3.1 Test 2

(a) (b)

Figure 84. Comparison in the frequency domain between the GNSS (in blue) and the accelerometric (in red) signals acquired in test 2 during the test: (a) peak frequencies due to the free oscillations generated by the first excitation; (b) peak frequencies due to the free oscillations generated by the second excitation.

Table 23. Results in the frequency domain of test 2 during the test.

Point	Frequencies 1				Frequencies 2			
	GNSS	Acc.	Diff.	Diff.	GNSS	Acc.	Diff.	Diff.
[-]	[Hz]	[Hz]	[Hz]	[%]	[Hz]	[Hz]	[Hz]	[%]
1	4.60	4.60	0.00	0.00	4.56	4.56	0.00	0.00
2	4.60	4.60	0.00	0.00	4.56	4.56	0.00	0.00
3	3.30	4.30	1.00	23.26	4.22	4.22	0.00	0.00
4	4.30	4.60	0.30	6.52	4.22	4.22	0.00	0.00
5	4.60	4.60	0.00	0.00	4.22	4.22	0.00	0.00
Average	4.28	4.54	0.26	5.96	4.36	4.36	0.00	0.00
Average (without point 3)	4.53	4.60	0.08	1.63	4.39	4.39	0.00	0.00

9.3.2 Test 3

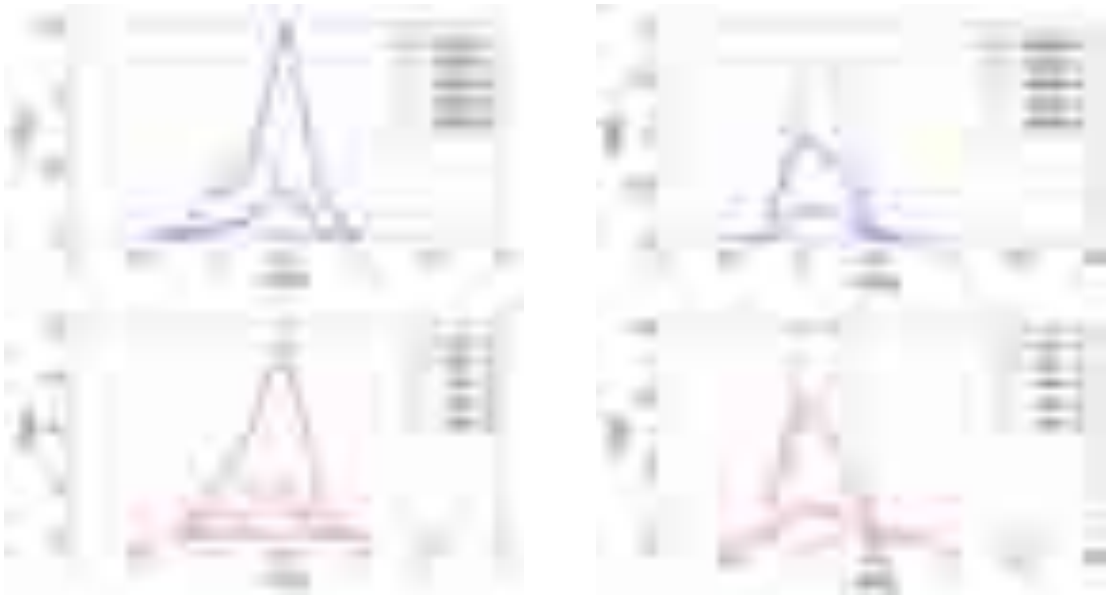

(a) (b)

Figure 85. Comparison in the frequency domain between the GNSS (in blue) and the accelerometric (in red) signals acquired in test 3 during the test: (a) peak frequencies due to the free oscillations generated by the first excitation; (b) peak frequencies due to the free oscillations generated by the second excitation.

Table 24. Results in the frequency domain of test 3 during the test.

Point	Frequencies 1				Frequencies 2			
	GNSS	Acc.	Diff.	Diff.	GNSS	Acc.	Diff.	Diff.
[-]	[Hz]	[Hz]	[Hz]	[%]	[Hz]	[Hz]	[Hz]	[%]
1	4.5	4.5	0.00	0.00	4.00	4.00	0.00	0.00
2	4.5	4.5	0.00	0.00	4.00	4.00	0.00	0.00
3	4.25	4.25	0.00	0.00	4.25	4.00	0.25	5.88
4	4.25	4.25	0.00	0.00	4.25	4.25	0.00	0.00
5	4.25	4.25	0.00	0.00	4.25	4.25	0.00	0.00
Average	4.35	4.35	0.00	0.00	4.15	4.10	0.05	1.18
Average (without point 3)	4.38	4.38	0.00	0.00	4.13	4.13	0.00	0.00

9.3.3 Test 4

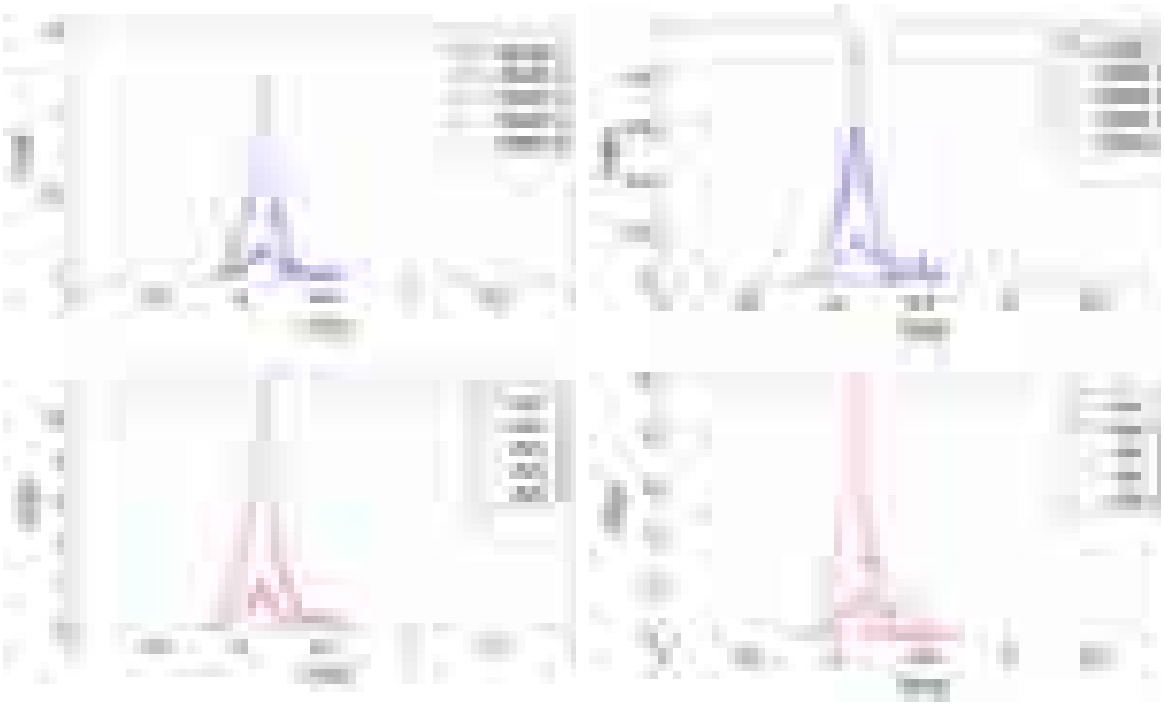

(a) (b)

Figure 86. Comparison in the frequency domain between the GNSS (in blue) and the accelerometric (in red) signals acquired in test 4 during the test: (a) peak frequencies due to the free oscillations generated by the first excitation; (b) peak frequencies due to the free oscillations generated by the second excitation.

Table 25. Results in the frequency domain of test 4 during the test.

Point	Frequencies 1				Frequencies 2			
	GNSS	Acc.	Diff.	Diff.	GNSS	Acc.	Diff.	Diff.
[-]	[Hz]	[Hz]	[Hz]	[%]	[Hz]	[Hz]	[Hz]	[%]
1	4.13	4.13	0.00	0.00	4.13	4.13	0.00	0.00
2	4.13	4.13	0.00	0.00	4.13	4.13	0.00	0.00
3	4.13	4.13	0.00	0.00	4.13	4.13	0.00	0.00
4	4.13	4.13	0.00	0.00	4.13	4.13	0.00	0.00
5	4.13	4.13	0.00	0.00	4.13	4.13	0.00	0.00
Average	4.13	4.13	0.00	0.00	4.13	4.13	0.00	0.00
Average (without point 3)	4.13	4.13	0.00	0.00	4.13	4.13	0.00	0.00

9.4 Script for log files reading

```
clear
close all
clc

dirn = 'test160421/2_sx'; %directory used to create structure logfiles
logfiles = dir([dirn '/' '*.LOG']); %structure that contains characericstics of log files
for kf=1:length(logfiles) %reading each log file
    disp(['file #' int2str(kf) ' ' logfiles(kf).name]) %shows which log file is considered
in iteration
    fname=logfiles(kf).name; %name of log file considered in iteration
    if kf==1 %do it only for first iteration
        eval(['cd ' dirn]) %go to directory where log files are
    end
    kk=1; %counter
    FC=readcell(fname); %creates cell array by reading from file "fname"
    for ii=1:length(FC) %considers each row of FC
        FCappo=[]; %auxiliar cell array
        for jj=1:length(FC(ii,:)) %considers each column of FC
            if max(size(FC{ii,jj}))>1
                FCappo=[FCappo ',' FC{ii,jj}];
            elseif and(max(size(FC{ii,jj}))==1,isfloat(FC{ii,jj}))
                FCappo=[FCappo ',' num2str(FC{ii,jj},15)];
            end
        end

        % ANALYSE CELL ARRAY
        if isempty(FCappo)
            appo=false;
        else
            appo=contains(FCappo,'BESTPOSA');
        end
        if (appo==1)
            i1=strfind(FCappo,'NARROW_INT,'); %find where the coordinate string start
            i2=strfind(FCappo,'BESTPOSA'); %find where the time string start
            if (isempty(i1)||isempty(i2)) %check if there is no coordinate and time string
                continue
            end

            % TIME
            timeString=FCappo(i2:i1); %write the string that contain the time data
            ic1=find(timeString==','); %find the the index of comma that divide the data
            tempo(kk,1)=str2num(timeString(ic1(6)+1:ic1(7)-1)); %find the time data

            % COORDINATES
            coordinateString=FCappo(i1+11:i1+100); %write the string that contain the
coordinate data
            ic2=find(coordinateString==','); %find the index of comma that divide the data
            lat(kk,1)=str2num(coordinateString(1:ic2(1)-1)); %find the latitude data
            lon(kk,1)=str2num(coordinateString(ic2(1)+1:ic2(2)-1)); %find the longitude
data
            alt(kk,1)=str2num(coordinateString(ic2(2)+1:ic2(3)-1)); %find the altitude data
```

```
            kk=kk+1; %increase counter
        end
    end

    % SAVE DATA
    save(fname(1:end-4),'tempo','lat','lon','alt')
    varsc={'tempo','lat','lon','alt','FC'};
    clear(varsc{:});
end
```

Published with MATLAB® R2020b

9.5 Script for geodetic coordinates conversion

```
function [t,lam,phi,h,x,y,z,xEast,yNorth,zUp,xLocal,yLocal,zLocal] = ...
    dataConverter(fname)
%The function applies a coordinates' transformation. It takes as input the
%name of a file (string) which contains the variables tempo, lat, lon and
%alt. Those vaiables are respetively the time, latitude, longitude and
%altitude acquired from a Novatel sensor. The function gives back as output
%the coordinates expressed in three different reference system, which are
%the ECEF (Earth Centred Earth Fixed reference system), the ENU (Eastn
%North Up reference system) and the LOCAL reference system. The first two
%can be found in literature, the third one is the local reference system
%applied to the structure that is being analysed. It is tangent to the
%structure as the ENU referencesystem. The only difference is that the
%local one is rotated around the vertical axis of an angle specified by the
%user.
%fname = string that specifies the name of the file
%t = time vector
%lam = latitude vector
%phi = longitude vector
%h = altitude vector
%x = x vector in ECEF
%y = y vector in ECEF
%z = z vector in ECEF
%xEast = East vector in ENU
%yNorth = North vector in ENU
%zUp = Up vector in ENU
%xLocal = x vector in LOCAL
%yLocal = y vector in LOCAL
%zLocal = z vector in LOCAL

load(fname,'t','lam','phi','h')

% geo2ecef
% changing coordinates from GEODETIC to ECEF
wgs84 = wgs84Ellipsoid;
L = length(t); %number of acquisitions
ECEF = zeros(L,3); %matrix of ECEF coordinates
for ii=1:L %acquisitions
    [ECEF(ii,1),ECEF(ii,2),ECEF(ii,3)] =...
        geodetic2ecef(wgs84,lam(ii),phi(ii),h(ii));
end
x = ECEF(:,1);
y = ECEF(:,2);
z = ECEF(:,3);

% ecef2enu
% changing coordinates from ECEF to ENU
LAT0 = mean(lam); %refernece latitude in ENU plane
LON0 = mean(phi); %reference longitude in ENU plane
H0 = mean(h); %reference altitude in ENU plane
ENU = zeros(L,3); %matrix of ENU coordinates
for ii=1:L
```

```
    [ENU(ii,1),ENU(ii,2),ENU(ii,3)] = ...
        ecef2enu(x(ii),y(ii),z(ii), LAT0, LON0, H0, wgs84);
end
xEast = ENU(:,1);
yNorth = ENU(:,2);
zUp = ENU(:,3);

% enu2local
% changing coordinates from ENU to LOCAL
alpha = -14;
alpha_radians = alpha * pi/180;
LOCAL = zeros(L,3);
for ii = 1:L
    LOCAL(ii, :) = [xEast(ii)*cos(alpha_radians) - ...
        yNorth(ii)*sin(alpha_radians) xEast(ii,1)*sin(alpha_radians) + ...
        yNorth(ii)*cos(alpha_radians) zUp(ii)];
end
xLocal = LOCAL(:,1);
yLocal = LOCAL(:,2);
zLocal = LOCAL(:,3);
```

Published with MATLAB® R2020b

9.6 Script for data filtering

```
function [y,B,A]=bandpassfilter(Fi,Ff,n,u,Fc)
%function [y,B,A]=bandpassfilter(Fi,Ff,n,u,Fc);
%y= segtnale filtrato
%Fi frequenza iniziale del filtro passa banda
%Ff frequenza finale del filtro passabanda
%n ordine del filtro
%Fc frequenza di campionamento

freqi=Fi/(Fc/2);
freqf=Ff/(Fc/2);
[B,A]=butter(n,[freqi,freqf]);
y=filtfilt(B,A,u);
```

Published with MATLAB® R2020b

10 Bibliography

1. Larocca APC, de Araújo Neto JO, Trabanco JLA, dos Santos MC, Barbosa ACB. First Steps Using Two GPS Satellites for Monitoring the Dynamic Behavior of a Small Concrete Highway Bridge. Journal of Surveying Engineering [Internet]. 2016 Aug;142(3). Available from: https://ascelibrary.org/doi/10.1061/%28ASCE%29SU.1943-5428.0000170
2. Moschas F, Stiros S. Measurement of the dynamic displacements and of the modal frequencies of a short-span pedestrian bridge using GPS and an accelerometer. Eng Struct [Internet]. 2011;33(1):10–7. Available from: http://dx.doi.org/10.1016/j.engstruct.2010.09.013
3. Limongelli MP, Çelebi M. Seismic Structural Health Monitoring. Limongelli MP, Çelebi M, editors. Springer Tracts in Civil Engineering [Internet]. 2019 [cited 2022 Feb 17];447. Available from: http://link.springer.com/10.1007/978-3-030-13976-6
4. Rainieri C, Fabbrocino G. Operational Modal Analysis of Civil Engineering Structures. 1st ed. Operational Modal Analysis of Civil Engineering Structures. Springer New York; 2014. 322 p.
5. Kaloop MR, Elbeltagi E, Wan Hu J, Elrefai A. Recent Advances of Structures Monitoring and Evaluation Using GPS-Time Series Monitoring Systems: A Review. International Journal of Geo-Information [Internet]. 2017; Available from: www.mdpi.com/journal/ijgi
6. Li X, Wang B, Li X, Huang J, Lyu H, Han X. Principle and performance of multi-frequency and multi-GNSS PPP-RTK. Satellite Navigation [Internet]. 2022;3(1). Available from: https://doi.org/10.1186/s43020-022-00068-0
7. Katsigianni G, Loyer S, Perosanz F. PPP and PPP-AR Kinematic Post-Processed Performance of GPS-Only, Galileo-Only and Multi-GNSS. Remote Sens (Basel) [Internet]. 2019 Oct 24;11(21):2477. Available from: https://www.mdpi.com/2072-4292/11/21/2477

8. Glaner M, Weber R. PPP with integer ambiguity resolution for GPS and Galileo using satellite products from different analysis centers. GPS Solutions [Internet]. 2021;25(3):1–13. Available from: https://doi.org/10.1007/s10291-021-01140-z
9. European GNSS Agency. PPP-RTK market and technology report [Internet]. Vol. b. 2019. Available from: https://www.euspa.europa.eu/simplecount_pdf/tracker?file=calls_for_proposals/rd.03_-_ppp-rtk_market_and_technology_report.pdf
10. C. Fu C, Zhu Y, Hou KY. Utilization of Dynamic and Static Sensors for Monitoring Infrastructures. In: Marghany M, editor. Advanced Remote Sensing Technology for Synthetic Aperture Radar Applications, Tsunami Disasters, and Infrastructure [Internet]. 1st ed. IntechOpen; 2019. p. 182. Available from: undefined/state.item.id
11. Han H, Wang J, Meng X, Liu H. Analysis of the dynamic response of a long span bridge using GPS/accelerometer/anemometer under typhoon loading. Eng Struct [Internet]. 2016;122:238–50. Available from: http://dx.doi.org/10.1016/j.engstruct.2016.04.041
12. Capellari G, Chatzi E, Mariani S. Cost–Benefit Optimization of Structural Health Monitoring Sensor Networks. Sensors [Internet]. 2018 Jul 6;18(7):22. Available from: http://www.mdpi.com/1424-8220/18/7/2174
13. Kaloop MR, Li H. Multi input-single output models identification of tower bridge movements using GPS monitoring system. Measurement (Lond) [Internet]. 2014;47(1):531–9. Available from: http://dx.doi.org/10.1016/j.measurement.2013.09.046
14. Notti D, Cina A, Manzino A, Colombo A, Bendea IH, Mollo P, et al. Low-Cost GNSS Solution for Continuous Monitoring of Slope Instabilities Applied to Madonna Del Sasso Sanctuary (NW Italy). Sensors [Internet]. 2020 Jan 4;20(1):23. Available from: https://www.mdpi.com/1424-8220/20/1/289
15. Pehlivan H. Frequency analysis of GPS data for structural health monitoring observations. Structural Engineering and Mechanics [Internet]. 2018;66(2):185–93. Available from: http://www.techno-press.org/content/?page=article&journal=sem&volume=66&num=2&ordernum=4

16. Moschas F, Stiros S. Dynamic Deflections of a Stiff Footbridge Using 100-Hz GNSS and Accelerometer Data. Journal of Surveying Engineering [Internet]. 2015;141(4):8. Available from: https://ascelibrary.org/doi/10.1061/%28ASCE%29SU.1943-5428.0000146
17. Ozer Yigit C, Gurlek E. Experimental testing of high-rate GNSS precise point positioning (PPP) method for detecting dynamic vertical displacement response of engineering structures. Geomatics, Natural Hazards and Risk [Internet]. 2017;8(2):893–904. Available from: https://www.tandfonline.com/doi/full/10.1080/19475705.2017.1284160
18. Kaloop MR, Hu JW, Elbeltagi E. Adjustment and assessment of the measurements of low and high sampling frequencies of GPS real-time monitoring of structural movement. ISPRS Int J Geoinf [Internet]. 2016;5(12):16. Available from: https://www.mdpi.com/2220-9964/5/12/222
19. Wang X, Zhao Q, Xi R, Li C, Li G, Li L. Review of Bridge Structural Health Monitoring Based on GNSS: From Displacement Monitoring to Dynamic Characteristic Identification. IEEE Access [Internet]. 2021;9:80043–65. Available from: https://ieeexplore.ieee.org/document/9440896/
20. Portland State Aerospace Society. Conversion of Geodetic coordinates to the Local Tangent Plane. Earth. 2007;01.
21. Coordinate Systems (Spatial Reference Systems) [Internet]. [cited 2021 Nov 16]. Available from: https://docs.oracle.com/cd/A91202_01/901_doc/appdev.901/a88805/sdo_cs_c.htm
22. Ruffhead A, Whiting BM. Surveying Working Paper No 01 / 2020 Introduction to geodetic datum transformations and. 2020;(October).
23. Heiskanen Moritz 1967 Physical Geodesy : San Francisco W. H. Freeman and Company : Free Download, Borrow, and Streaming : Internet Archive [Internet]. [cited 2021 Nov 18]. Available from: https://archive.org/details/HeiskanenMoritz1967PhysicalGeodesy/page/n191/mode/2up

24. Wang Y, Huynh G, Williamson C. Integration of Google Maps/Earth with microscale meteorology models and data visualization. Comput Geosci. 2013;61:23–31.